Journal of the Physical Society of Japan **94**, 031005 (2025)
https://doi.org/10.7566/JPSJ.94.031005

Self-Energy Spectroscopy and Artificial Neural Network

Youhei Yamaji*

Research Center for Materials Nanoarchitectonics (MANA), National Institute for Materials Science (NIMS), Tsukuba, Ibaraki 305-0044, Japan

(Received September 19, 2024; revised January 14, 2025; accepted January 14, 2025; published online February 26, 2025)

The analysis of spectroscopy data has played an important role in untangling the complex dynamics of many-body electrons in quantum materials and making their emergent properties understandable. Spectroscopy measurements provide us with the responses of the many-body electrons in materials when energy and momentum are injected. These responses have been analyzed using a single-particle picture augmented by *self-energy*, which quantifies the deviation from simple free fermion excitation. While the self-energy is not directly observed in spectroscopy, it has been extracted from the obtained spectra by solving inverse problems. Especially, for superconductors, the analysis of self-energy is a key to understanding the origin of the superconductivity. The recent rise of machine learning has served to update the self-energy analysis of spectroscopy data and opened a new avenue for understanding the entangled nature of many-body electrons. In this article, self-energy analysis using the flexibility of neural networks is reviewed and positioned in the research trajectory from Bardeen–Cooper–Schrieffer superconductors to copper-oxide high-temperature superconductors.

1. Introduction

In condensed matter physics community, the rise of materials informatics[1] has sparked renewed interest in Bayesian approaches[2] and machine learning methods,[3] which have emerged alongside the rapid development of deep learning, leading to the current rise of generative artificial intelligence. Such interests have further expanded into various research fields, such as computer vision including image processing, natural language processing, and speech processing, as Bayesian and machine learning approaches have been developed across multiple disciplines.

Even though usage of large database has attracted considerable attention, such as virtual screening or recommendation of synthesizable materials on databases consisting of large amount of experimental data and synthetic data generated by simulation,[4] analysis of a small set of data (higher dimensional but from a single or several materials) has been actively studied in the current research trend. While the former data-driven approaches, such as exploration of structure-property correlations, have been augmented by the databases and automated simulation,[5] it is also interesting to untangle information encoded in the experimental observation of a single material by utilizing a broader range of theoretical or numerical tools, whose range has been expanded by the Bayesian approaches and machine learning.

An important direction of machine-learning approaches is to find principal components, or extract a low-rank structure crucial to structure-property correlations, from the given data, which have been, in certain instances, represented by an incomplete matrix or tensor. Irrespectively of supervised or unsupervised learning, it is important to extract these principal components, which may be called control parameters, reaction coordinates, or a latent space, depending on the context. These are not only axes, curves, or surfaces in a vector space $\mathbb{R}^d$ but also basis functions in a Hilbert space.

The extracted principal components may improve interpretation of data, as in the standard principal component analysis while the low-rank structures have been used for prediction of missing data. The automation of the research processes is also augmented by boosting interpretation process of the given data when human involvement can become a bottleneck. New interpretation of old problems is expected, as well.

The machine learning and related approaches have also attracted attention as generators of complicated (probability) distributions, which are useful in condensed matter physics. Indeed, probability distributions generated by machine-learning approaches have been used to imitate underlying probability distributions of many-body configuration in variational wave function[6] and self-learning Monte Carlo methods.[7] The generation of complicated probability distribution itself have been sophisticated under mutual influence between studies on neural networks and many-body physics, which results in, for example, neural canonical transformations.[8]

In the present article, we focus on spectroscopy of quantum materials as an example of research fields where traditional theoretical tools to analyze spectra have been developed alongside the recent development inspired by machine-learning approaches. The spectroscopy provides us with energy-dependent materials' responses to external perturbation, which often contain crucial information such as charge gap in superconductors and origin of superconductivity.[9]

When we visually examine a crystalline sample, we can qualitatively speculate whether it conducts electric current based on its appearance, such as whether it is transparent, black, or exhibits a metallic luster. These characteristics are related to the material's response to incident light, which often provides us with clues to understand behaviors of electrons confined in the crystal. (Here, surface structures of the materials may also influence the response more than intrinsic properties of electrons inside.)

To access quantitative information encoded in these responses, sophisticated technologies for spectroscopy have been developed alongside theoretical tools to analyze observed spectra. Absorption or photoluminescence has been studied not only with visible light but also with electromagnetic waves beyond the visible light range. Neutrons or other particles have been also utilized. Materials may absorb energy $\hbar\omega$ and momentum $\hbar\boldsymbol{k}$ (in the following we set $\hbar = 1$)

from incident particles, while they may emit electrons in response to the absorbed energy and momentum. The tunneling phenomena of electrons has been also utilized for spectroscopy.

Indeed, many-body electrons in crystalline solids have been a proving ground for spectroscopy and related theoretical tools. Experimental technologies and theoretical tools for inelastic x-ray and neutron scattering, tunneling measurement, and photoemission spectroscopy have been developed through the application to correlated electrons in quantum materials such as superconductors, topological materials, and so on. To interpret spectroscopy data, in cooperation with the development of *forward* approaches, *inverse* approaches have been studied since the 1960s as well.

While we will focus on many-body effects in spectroscopy, which will be introduced in the following, there are various machine-learning approaches on analysis of spectroscopy data, which are beyond the scope of the present article. To remove human involvement or replace intuitive but biased model, machine learning approaches have been introduced, which are expected to accelerate the data analysis. There have been studies to make automatic analysis of the huge spectroscopic data possible.[10,11] To improve spectroscopy data itself, the machine learning approaches have been introduced. Denoising of the photoemission spectroscopy data[12,13] is an example. Deep neural networks have been also utilized to remove structured noise in the photoemission data[14] as well. Aside from significant influence of statistical mechanics on the early stage of the development of the machine learning, including neural networks, the Bayesian approaches have been utilized in condensed matter physics, even though frequentist statistics had been taught as the standard approach in undergraduate and graduate schools. An example is the maximum entropy method in the analytical continuation.[15] The Bayesian approaches in analytic continuation have been further developed.[16]

The present article is organized as follows. In Sect. 2, we review the theoretical representation of many-body electron systems, covering topics from many-body wave functions to the self-energy function, an analytical function that encodes the effects of many-body interactions, interconnected through the Green function formalism. Then, in Sect. 3, several self-energy models are introduced. To analyze a category of Bardeen–Cooper–Schrieffer-type superconductors where electrons strongly interact with quantized vibration of ions forming crystals, physicists had combined forward problem with inverse problem to extract many-body nature of many-body electrons. To analyze high-temperature superconductors, in which mutual Coulomb repulsion among electrons becomes relevant, further self-energy models, including neural network representations, will be introduced. The applications of the self-energy models to spectroscopy data is reviewed in Sect. 4. Section 5 is devoted to summary and future perspectives.

2. Many-body Effects in Spectroscopy

Electrons confined solids are typical examples of quantum many-body systems. Starting from the few electrons in atoms and small molecules,[17,18] the many-body electron systems have been targets of intensive researches.[19] Magnetism and superconductivity are typical examples of phenomena emerging in the many-body electrons. Nowadays, from the quantum-information point view, properties of the many-body electrons originating from structures of the quantum entanglement attract attention. Especially, topological many-body states of matters have been intensively studied.

However, even in a simple many-body electron system, analysis of the wave function will be complicated, as follows. First of all, the many-body Schrödinger equation for the many-body electrons is hard to solve even for few electrons confined around a nuclear and even when the quantum nature of the nuclear is ignored (Born–Oppenheimer approximation). Naively speaking, we may map the many-body Schrödinger equation to a (generalized) eigenvalue problem for a sparse Hamiltonian matrix. For the sake of simplicity, we focus on non-relativistic systems in the following. When we consider $N_{\rm orb}$ single-particle orbitals and $N_{\rm e}$ electrons, the linear dimension of the Hamiltonian matrix is $(2N_{\rm orb})!/N_{\rm e}!/(2N_{\rm orb}-N_{\rm e})!$, where the factor 2 comes from the spin degrees of freedom of electrons. If you know the quantum numbers, such as total spin/angular momentum for electrons confined in an atom or the total momentum for electrons confined in a crystalline solid, you can reduce the linear dimension. However, in general, the dimension of the matrix grows exponentially when $N_{\rm orb}$ or $N_{\rm e}$ increases. Thus, researchers have tried to find smart way to truncate the basis set or introduced approximations.

Even when we obtain the many-body eigenstate wave functions, $|\Phi\rangle$, the wave functions themselves would be a kind of the black box that generates a probability amplitude as an output from given the location of the electrons as input data. Let us introduce one of the simplest example, interacting $S = 1/2$ spins, or qubits, described by simple effective Hamiltonians, such as the Heisenberg Hamiltonian. The Heisenberg Hamiltonian effectively describes insulating phases of hydrogen crystals in Mott's gedanken experiment[20] and La_2CuO_4.[21] For example, the many-body wave function of the 36 spins is naively represented by a 2^{36} dimensional complex vector, which would require 1 TiB (1024^4 bytes) of storage. Each element of the vector represents the probability amplitude for a given spin configuration.

Then, how do we understand the properties of and extract useful information from the wave function? In the history of the many-body physics, there have been seminal works that succeed to make the black box (at least partially) white. Typical examples of them would be the roton theory[22–24] for liquid helium 4 and the Fermi liquid theory,[25,26] originally for liquid helium 3 but later applied to other many-body fermion systems, including many-body electrons in metals.

These theories explain what happens in a many-body system when energy and momentum are injected. The Fermi liquid theory states that a series of excited states are labeled by a particle-like excitation with energy $\delta\epsilon$ measured from the ground state and many-body momentum $\boldsymbol{k}$. Here, the momentum appears in the phase factor of the eigenvalue of the operator $\hat{T}_{\boldsymbol{\delta}}$ that translates the system with an interval $\boldsymbol{\delta}$ as $\hat{T}_{\boldsymbol{\delta}}|\Phi\rangle = e^{+i\boldsymbol{k}\cdot\boldsymbol{\delta}}|\Phi\rangle$.

Let us introduce a concrete description of many-body quantum systems. As the simplest example, we first focus on an electron gas, defined by the following Hamiltonian,

$$\hat{H} = -\sum_{\sigma}\int d^3r\,\frac{1}{2m_{\mathrm{e}}}\hat{\phi}^{\dagger}_{\sigma}(\boldsymbol{r})\nabla^2\hat{\phi}_{\sigma}(\boldsymbol{r}) + \sum_{\sigma}\int d^3r\,\hat{\phi}^{\dagger}_{\sigma}(\boldsymbol{r})v_{\mathrm{ext}}(\boldsymbol{r})\hat{\phi}_{\sigma}(\boldsymbol{r}) + \sum_{\sigma,\sigma'}\int d^3r\int d^3r'\,\frac{\hat{\phi}^{\dagger}_{\sigma}(\boldsymbol{r})\hat{\phi}_{\sigma}(\boldsymbol{r})\hat{\phi}^{\dagger}_{\sigma'}(\boldsymbol{r}')\hat{\phi}_{\sigma'}(\boldsymbol{r}')}{2\epsilon|\boldsymbol{r}-\boldsymbol{r}'|}, \quad (1)$$

where m_{e} is the electron mass, v_{ext} is the external electrostatic potential, ϵ is the dielectric constant, and $\hat{\phi}(\boldsymbol{r})$ is the field operator given by

$$\hat{\phi}_{\sigma}(\boldsymbol{r}) = V^{-1/2}\sum_{\boldsymbol{k}} e^{+i\boldsymbol{k}\cdot\boldsymbol{r}}\hat{c}_{\boldsymbol{k}\sigma}. \quad (2)$$

Here, $\hat{c}^{\dagger}_{\boldsymbol{k}\sigma}$ ($\hat{c}_{\boldsymbol{k}\sigma}$) is the creation (annihilation) operator for an electron with spin σ and momentum $\boldsymbol{k}$. We assume that electrons are in a cube of volume V with periodic boundary conditions. The external potential v_{ext} is constant in the electron gas.

In many cases, we can assume that the ground state wave function $|\Phi_0\rangle$ has zero momentum or is translationally invariant as $\hat{T}_{\boldsymbol{\delta}}|\Phi_0\rangle = |\Phi_0\rangle$. Then, a simple way to construct a state with finite momentum is, for example, adding an electron with $\boldsymbol{k}$ to the ground state as $\hat{c}^{\dagger}_{\boldsymbol{k}\sigma}|\Phi_0\rangle$. Indeed, the state has finite momentum $\boldsymbol{k}$ as $\hat{T}_{\boldsymbol{\delta}}(\hat{c}^{\dagger}_{\boldsymbol{k}\sigma}|\Phi_0\rangle) = e^{+i\boldsymbol{k}\cdot\boldsymbol{\delta}}\hat{c}^{\dagger}_{\boldsymbol{k}\sigma}|\Phi_0\rangle$.

When we follow the dynamics of such a state with finite momentum, we can introduce a Green function that describes the propagation of a single particle or single hole as

$$G_{\sigma}(\boldsymbol{k},\omega) = \langle\Phi_0|\hat{c}_{\boldsymbol{k}\sigma}\frac{1}{\omega+i\eta+\mu-\hat{H}+E_0}\hat{c}^{\dagger}_{\boldsymbol{k}\sigma}|\Phi_0\rangle + \langle\Phi_0|\hat{c}^{\dagger}_{\boldsymbol{k}\sigma}\frac{1}{\omega+i\eta+\mu+\hat{H}-E_0}\hat{c}_{\boldsymbol{k}\sigma}|\Phi_0\rangle \quad (3)$$

$$= \sum_{m}\frac{\langle\Phi_0|\hat{c}_{\boldsymbol{k}\sigma}|m^{N_{\mathrm{e}}+1}\rangle\langle m^{N_{\mathrm{e}}+1}|\hat{c}^{\dagger}_{\boldsymbol{k}\sigma}|\Phi_0\rangle}{\omega+i\eta+\mu-E_m^{N_{\mathrm{e}}+1}+E_0} + \sum_{n}\frac{\langle\Phi_0|\hat{c}^{\dagger}_{\boldsymbol{k}\sigma}|n^{N_{\mathrm{e}}-1}\rangle\langle n^{N_{\mathrm{e}}-1}|\hat{c}_{\boldsymbol{k}\sigma}|\Phi_0\rangle}{\omega+i\eta+\mu+E_n^{N_{\mathrm{e}}-1}-E_0}, \quad (4)$$

where E_0 is the ground state energy that satisfies $\hat{H}|\Phi_0\rangle = E_0|\Phi_0\rangle$ and η is a positive broadening factor. Here, $E_m^{N_{\mathrm{e}}+1}$ is an eigenvalue corresponding to an $N_{\mathrm{e}}+1$ electron eigenstate $|m^{N_{\mathrm{e}}+1}\rangle$ of $\hat{H}$ while $E_n^{N_{\mathrm{e}}-1}$ is an eigenvalue corresponding to an $N_{\mathrm{e}}-1$ electron eigenstate $|n^{N_{\mathrm{e}}-1}\rangle$ of $\hat{H}$. From the construction above, the Green function is an analytic complex function represented by the summation of poles of order at most one. When we take the *retarded representation* as in Eq. (4), these poles are located in the lower half plane.

By introducing a single-particle dispersion $\epsilon(\boldsymbol{k})$, we can transform the Lehmann representation Eq. (4) as,

$$G_{\sigma}(\boldsymbol{k},\omega) = \frac{1}{\omega+i\eta+\mu-\epsilon(\boldsymbol{k})-\Sigma(\boldsymbol{k},\omega)}, \quad (5)$$

where $\Sigma(\boldsymbol{k},\omega)$ is a *self-energy* that encodes deviation from the single particle picture, and satisfies the following relation,

$$\Sigma(\boldsymbol{k},\omega) = -\frac{1}{\pi}\int d\omega'\,\frac{\mathrm{Im}\,\Sigma(\boldsymbol{k},\omega')}{\omega+i\eta-\omega'} \quad (6)$$

$$= \frac{1}{\pi}\int d\omega'\,\frac{\mathcal{P}(\boldsymbol{k},\omega')}{\omega+i\eta-\omega'}. \quad (7)$$

Here, $\mathcal{P}(\boldsymbol{k},\omega)$ is a positive definite distribution. We note that there is an ambiguity in the choice of the single-particle dispersion; The ω independent part of the self-energy, for example, the Hartree term, can be absorbed in $\epsilon(\boldsymbol{k})$.

By extracting the imaginary part of the Green function, we obtain the momentum and energy resolved density of states, $A(\boldsymbol{k},\omega) = -(1/\pi)\,\mathrm{Im}\,G(\boldsymbol{k},\omega)$, called a spectral weight or spectral function. As discussed in the following sections, photoemission ($\omega \lesssim 0$) and inverse photoemission ($\omega \gtrsim 0$) spectroscopy enable us to access the spectral function.[27,28]

Even when the mutual Coulomb repulsion is strong, if a pole at $\omega = \epsilon(\boldsymbol{k}_{\mathrm{F}}) - \mu - i\eta$ has a finite residue Z defined by

$$Z^{-1} = 1 - \frac{\partial}{\partial\omega}\mathrm{Re}\,\Sigma(\boldsymbol{k}_{\mathrm{F}},\omega)\Big|_{\omega=0}, \quad (8)$$

the Fermi liquid theory is valid. Here, we note that the residue Z is the weight of the particle-like excitation.

In the homogeneous electron gas, the bare single-particle dispersion, $\epsilon(\boldsymbol{k}) = |\boldsymbol{k}|^2/2m_{\mathrm{e}}$, will be renormalized due to the Coulomb repulsion. By introducing the effective mass,

$$m^* = \frac{1-\frac{\partial}{\partial\omega}\mathrm{Re}\,\Sigma(\boldsymbol{k}_{\mathrm{F}},\omega)\Big|_{\omega=0}}{\frac{1}{m_{\mathrm{e}}}+\frac{1}{k_{\mathrm{F}}}\frac{\partial}{\partial k}\mathrm{Re}\,\Sigma(\boldsymbol{k}_{\mathrm{F}},\omega)\Big|_{\omega=0}}, \quad (9)$$

we can approximate the original Green function as,

$$G_{\sigma}(\boldsymbol{k},\omega) \simeq \frac{Z}{\omega+i/\tau(\boldsymbol{k},\omega)-\frac{k_{\mathrm{F}}}{m^*}(|\boldsymbol{k}|-k_{\mathrm{F}})} + (\text{incoherent part}). \quad (10)$$

Here, the life time of the particle-like excitation $\tau(\boldsymbol{k},\omega)$ defined as $1/\tau(\boldsymbol{k},\omega) = -Z\,\mathrm{Im}\,\Sigma(\boldsymbol{k},\omega)$, which is expanded as $1/\tau_0 + \beta\omega^2$ around $\omega\sim 0$. Then, we can interpret the Green function as follows: A plane wave of $|\boldsymbol{k}| \sim k_{\mathrm{F}}$ propagates with the renormalized k_{F}/m^* and decays into other plane waves with a life time τ.

The incoherent part shows rich structure in many-body systems. In the homogeneous electron gas, plasmon satellites or sidebands[29] are generated by dressed single-particle excitations involving plasmons in addition to the renormalized quasiparticle excitations.[30,31]

When we describe crystalline solids, we may introduce a different basis set, instead of the plane waves in the vacuum. A typical choice is Wannier orbitals often localized around the ions. It has been known that a subspace expanded by a small subset of the Wannier orbitals will be relevant to the low- to room-temperature properties of the solid. When one performs photoemission spectroscopy and, thus, extract an electron from the solid as discussed in the following sections, one need to pay attention to the matrix element between the Wannier orbitals and plane waves. The Wannier orbitals are also relevant to scanning tunneling spectroscopy.[36]

In the periodic crystals, it is convenient to separate a wave number into a wave number in the first Brillouin zone $\boldsymbol{k}$ and a reciprocal lattice vector $\boldsymbol{G}$ as $\boldsymbol{k} \to \boldsymbol{k}+\boldsymbol{G}$. Then, the field operator $\hat{\phi}_{\sigma}(\boldsymbol{r})$ is rewritten by introducing a set of the Wannier orbitals, $\{\phi_{i\boldsymbol{R}}(\boldsymbol{r})\}$, as,

$$\hat{\phi}_{\sigma}(\boldsymbol{r}) = \sum_{w,\boldsymbol{R}}\phi_{w\boldsymbol{R}}(\boldsymbol{r})\hat{d}_{w\boldsymbol{R}\sigma}, \quad (11)$$

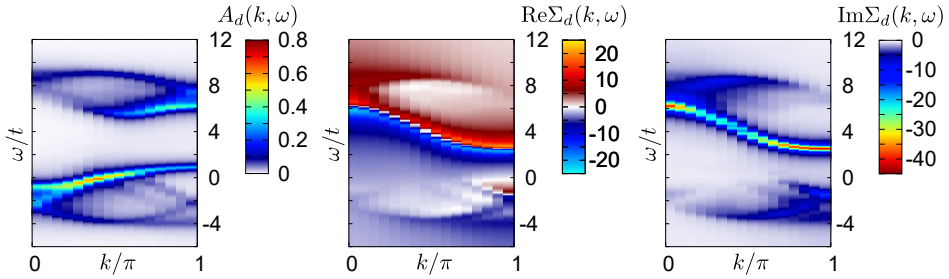

Fig. 1. (Color online) Spectral function and self-energy for a one-dimensional Hubbard Hamiltonian. The spectral function $A_d(k,\omega)$ for $U/t = 8$ and 32 sites with 28 electrons is shown in the left most panel, which is obtained by dynamical variational Monte Carlo methods.[32] Here, the broadening factor is set to $\eta/t = 0.125$. The real and imaginary part of the retarded Green function, $\Sigma_d(k,\omega)$, are shown in the middle and right most panels, respectively. A simple spectrum from the bare band dispersion, $(\eta/\pi)/[(\omega+\mu+2t\cos k)^2+\eta^2]$, is significantly modified by $\Sigma_d(k,\omega)$. There are several features in correlated electrons, such as Hubbard bands, spinon and holon branches.[33–35]

where $\phi_{w\boldsymbol{R}}(\boldsymbol{r})$ is the wth Wannier orbital in an unit labeled by the lattice $\boldsymbol{R}$. While the choice of the Wannier orbitals is not unique, the maximally localized Wannier orbitals[37,38] have been often employed in the literature. The creation (annihilation) operator for the plane wave in the vacuum, $\hat{c}^\dagger_{\boldsymbol{k}+\boldsymbol{G}\sigma}$ ($\hat{c}_{\boldsymbol{k}+\boldsymbol{G}\sigma}$), and that for the Wannier orbital, $\hat{d}^\dagger_{w\boldsymbol{R}\sigma}$ ($\hat{d}_{w\boldsymbol{R}\sigma}$) are transformed into each other through a unitary transformation as,

$$\hat{c}_{\boldsymbol{k}+\boldsymbol{G}\sigma} = \sum_{w,\boldsymbol{R}}\left[\int d^3r \frac{e^{-i(\boldsymbol{k}+\boldsymbol{G})\cdot\boldsymbol{r}}}{V^{1/2}}\phi_{w\boldsymbol{R}}(\boldsymbol{r})\right]\hat{d}_{w\boldsymbol{R}\sigma}. \tag{12}$$

In the series of the copper oxide superconductors, the electronic states around the Fermi level mainly consist of the Wannier orbitals consisting of Cu $3d_{x^2-y^2}$ atomic orbitals and O $2p_\sigma$ atomic orbitals[39] (see Refs. 40 and 41 as examples of the recent studies).

For ab initio single-orbital effective Hamiltonian, we may have a single Wannier orbital in each unit cell labeled by $\boldsymbol{R}$. Then, we simplify the index for the creation and annihilation operators, as $(w,\boldsymbol{R}) \to i$, where i is now a site index. Then, the ab initio single-orbital Hamiltonian is given by

$$\hat{H}_{\mathrm{eff}} = -\sum_{i,j,\sigma} t_{ij}\hat{d}^\dagger_{i\sigma}\hat{d}_{j\sigma} + U\sum_i \hat{n}_{i\uparrow}\hat{n}_{i\downarrow} + \frac{1}{2}\sum_{i\neq j} V_{i,j}(\hat{n}_{i\uparrow}+\hat{n}_{i\downarrow})(\hat{n}_{j\uparrow}+\hat{n}_{j\downarrow}), \tag{13}$$

where $\hat{n}_{i\sigma} = \hat{d}^\dagger_{i\sigma}\hat{d}_{i\sigma}$.

For simplicity, we rewrite the Green function by using the single Wannier orbital as,

$$\begin{aligned} G_\sigma(\boldsymbol{k},\omega) &= \langle\Phi_0|\hat{d}_{\boldsymbol{k}\sigma}\frac{1}{\omega+i\eta+\mu-\hat{H}_{\mathrm{eff}}+E_0}\hat{d}^\dagger_{\boldsymbol{k}\sigma}|\Phi_0\rangle \\ &\quad + \langle\Phi_0|\hat{d}^\dagger_{\boldsymbol{k}\sigma}\frac{1}{\omega+i\eta+\mu+\hat{H}_{\mathrm{eff}}-E_0}\hat{d}_{\boldsymbol{k}\sigma}|\Phi_0\rangle \\ &= \frac{1}{\omega+i\eta+\mu-\epsilon_d(\boldsymbol{k})-\Sigma_d(\boldsymbol{k},\omega)}, \end{aligned} \tag{14}$$

where $\boldsymbol{k}$ is a wave number in the first Brillouin zone and $\epsilon_d(\boldsymbol{k})$ is the single-particle dispersion obtained by the Fourier transformation of $-t_{ij}$.

By restricting ourself to one-dimensional lattice, and omitting the further neighbor t_{ij} other than the nearest neighbor hoppings t (>0) and the long-range effective Coulomb repulsion V_{ij}, we show an example of the self-energy $\Sigma_d(\boldsymbol{k},\omega)$ in Fig. 1. Here, the Green function is simply calculated by effectively constructing excited states with one more or less electrons from the ground state $|\Phi_0\rangle$, by using a dynamical variational Monte Carlo method,[32] and, then, the self-energy is obtained through Eq. (14).

A simple spectral function from the bare band dispersion, $(\eta/\pi)/[(\omega+\mu+2t\cos k)^2+\eta^2]$, is significantly modified by $\Sigma_d(k,\omega)$. There are several features found in spectral functions of the one-dimensional correlated electrons, which are called the Hubbard bands, and spinon or holon branches.[33–35] While the results of the finite-size simulation of the Hubbard model are shown in Fig. 1, the accumulation of poles in self-energy at the thermodynamic limit generates branch-cut singularities in the spectral functions of the one-dimensional Hubbard model, as studied in the Tomonaga–Luttinger model.[42–44]

To describe many-body electrons in superconducting phases, we need to introduce several theoretical details, especially related to the number of electrons, as follows. For those not interested in these details, you may skip the following seven paragraphs and go directly to the paragraph that includes Eq. (25).

The seminal article by Yang[45] introduced a fundamental approach to examine superconductivity in a given ground-state wave function with a fixed number of electrons. As explained in Ref. 45, the two-particle density matrix plays an important role and is defined by

$$\rho^{\sigma_1\sigma_2\tau_1\tau_2}_{j_1j_2\ell_1\ell_2} = \frac{\langle\Phi_0|\hat{d}^\dagger_{j_1\sigma_1}\hat{d}^\dagger_{j_2\sigma_2}\hat{d}_{\ell_1\tau_1}\hat{d}_{\ell_2\tau_2}|\Phi_0\rangle}{\langle\Phi_0|\Phi_0\rangle}. \tag{15}$$

By combining the first four indices into the index $J = (j_1,\sigma_1,j_2,\sigma_2)$ and the last four indices into $L = (\ell_1,\tau_1,\ell_2,\tau_2)$, we can treat the density matrix as matrix $\rho_{JL} = \rho^{\sigma_1\sigma_2\tau_1\tau_2}_{j_1j_2\ell_1\ell_2}$. When the largest singular value of ρ_{JL} is proportional to the number of electrons N_{e}, an off-diagonal long-range order spontaneously emerges, corresponding to superconductivity. The largest-singular-value singular vector provides us with the spatial and internal structures of the superconducting pairs. However, it is difficult to relate the two-particle density matrix to the self-energy.

In a standard procedure to examine spontaneous symmetry breakings, a small symmetry breaking field is introduced. We can find a ground state wave function as a function of the system size and the small but finite symmetry breaking field. Then, there are two important limits: one is the thermodynamic limit, where $1/N_{\mathrm{e}}$ approaches zero; the other is the limit in which the amplitude of the symmetry-breaking field goes to zero. When we take the zero symmetry breaking field

limit after taking the thermodynamic limit, we can judge whether symmetry breaking spontaneously occurs.

When we want to examine the superconducting order, we may introduce the following symmetry breaking field $\epsilon\mathcal{J}_{\boldsymbol{k}}$ for a spin-singlet pairing,

$$\hat{H}_{\rm eff} \leftarrow \hat{H}_{\rm eff} - \epsilon \sum_{\boldsymbol{k}} (\mathcal{J}_{\boldsymbol{k}} \hat{d}_{\boldsymbol{k}\uparrow} \hat{d}_{-\boldsymbol{k}\downarrow} + \mathcal{J}_{\boldsymbol{k}}^* \hat{d}_{-\boldsymbol{k}\downarrow}^\dagger \hat{d}_{\boldsymbol{k}\uparrow}^\dagger). \tag{16}$$

The symmetry breaking field inevitably mixes the dynamics of ↑-spin (↓-spin) electrons with those of ↓-spin (↑-spin) holes. Then, the number of electrons is not fixed. The thermodynamic limit should be defined by the expectation value of the electron number operator, $\hat{N} = \sum_{j,\sigma} \hat{d}_{j\sigma}^\dagger \hat{d}_{j\sigma}$. The ground-state wave function discussed so far is based on a vacuum $|0\rangle$ and creation operators multiplied to the vacuum. When the spin-singlet superconducting pair in the low-energy subspace is examined according to the BCS theory, the vacuum $|0\rangle$ is often replaced by

$$|\mathrm{vac}\rangle = \prod_{\boldsymbol{k}} \hat{d}_{-\boldsymbol{k}\downarrow}^\dagger |0\rangle, \tag{17}$$

where the product of the creation operators is taken over the entire Brillouin zone. The ground state wave function is given in grand canonical form as

$$|\widetilde{\Phi}_0\rangle = \sum_{m\in\mathbb{Z}} \frac{|A_m|}{\sum_{m'\in\mathbb{Z}} |A_{m'}|^2} e^{2mi\varphi} |\Phi_0^{N_{\rm e}+2m}\rangle, \tag{18}$$

where $|\Phi_0^N\rangle$ is the normalized projection of the ground-state wave function onto the N electron sector, A_m is a coefficient, φ is a $U(1)$ phase, and $N_{\rm e} = \langle\widetilde{\Phi}_0|\hat{N}|\widetilde{\Phi}_0\rangle / \langle\widetilde{\Phi}_0|\widetilde{\Phi}_0\rangle$ is assumed to hold.

By introducing the grand-canonical ground-state wave function, $|\widetilde{\Phi}_0\rangle$, into the Green function in Eq. (14), we can calculate the properties of the superconducting states. However, there are more convenient formulations of the superconducting states based on the self-energy. We can begin with the Green function along the time axis,

$$G_\uparrow(\boldsymbol{k},t) = -i\theta(t)\langle\widetilde{\Phi}_0|[\hat{d}_{\boldsymbol{k}\uparrow}(t)\hat{d}_{\boldsymbol{k}\uparrow}^\dagger + \hat{d}_{\boldsymbol{k}\uparrow}^\dagger \hat{d}_{\boldsymbol{k}\uparrow}(t)]|\widetilde{\Phi}_0\rangle, \tag{19}$$

where the Heisenberg representation of the operators is defined as $\hat{d}_{\boldsymbol{k}\sigma}(t) = e^{i(\hat{H}_{\rm eff}-\mu\hat{N})t} \hat{d}_{\boldsymbol{k}\sigma} e^{-i(\hat{H}_{\rm eff}-\mu\hat{N})t}$. The Fourier transformation of $G_\uparrow(\boldsymbol{k},t)$, of course, reproduces a representation similar to Eq. (14). To take into account the mixture of the electron and hole dynamics, the Green function for the ↓-spin particles is given by,

$$G_\downarrow(-\boldsymbol{k},t) = -i\theta(t)\langle\widetilde{\Phi}_0|[\hat{d}_{-\boldsymbol{k}\downarrow}^\dagger(t)\hat{d}_{-\boldsymbol{k}\downarrow} + \hat{d}_{-\boldsymbol{k}\downarrow}\hat{d}_{-\boldsymbol{k}\downarrow}^\dagger(t)]|\widetilde{\Phi}_0\rangle. \tag{20}$$

Due to the symmetry breaking field $\epsilon\mathcal{J}_{\boldsymbol{k}}$, $G_\uparrow(\boldsymbol{k},t)$, and $G_\downarrow(-\boldsymbol{k},t)$ are not independent of each other. Furthermore, the real-time evolution of these Green functions inevitably involves the following anomalous Green functions,

$$F_{\uparrow\downarrow}(\boldsymbol{k},t) = -i\theta(t)\langle\widetilde{\Phi}_0|[\hat{d}_{\boldsymbol{k}\uparrow}(t)\hat{d}_{-\boldsymbol{k}\downarrow} + \hat{d}_{-\boldsymbol{k}\downarrow}\hat{d}_{\boldsymbol{k}\uparrow}(t)]|\widetilde{\Phi}_0\rangle, \tag{21}$$

and

$$F_{\downarrow\uparrow}(\boldsymbol{k},t) = -i\theta(t)\langle\widetilde{\Phi}_0|[\hat{d}_{-\boldsymbol{k}\downarrow}^\dagger(t)\hat{d}_{\boldsymbol{k}\uparrow}^\dagger + \hat{d}_{\boldsymbol{k}\uparrow}^\dagger\hat{d}_{-\boldsymbol{k}\downarrow}^\dagger(t)]|\widetilde{\Phi}_0\rangle. \tag{22}$$

For example, Ref. 46 examines the superconducting state with an explicit wave function and the Green functions along the imaginary time axis, as summarized in the article's Appendix.

Then, the four Green functions constitute the Nambu representation[47] of the Green function,

$$\hat{G}(\boldsymbol{k},t) = \begin{bmatrix} G_\uparrow(\boldsymbol{k},t) & F_{\uparrow\downarrow}(\boldsymbol{k},t) \\ F_{\uparrow\downarrow}(\boldsymbol{k},t) & G_\downarrow(-\boldsymbol{k},t) \end{bmatrix}. \tag{23}$$

While the Fourier transformation of the Green function matrix may provide us with the spectral (Lehmann) representation as in Eq. (14), the time evolution of the Green function matrix may offer another representation.

To gain insight into the Green function matrix, we can examine the non-interacting limit. When U and V_{ij} are set to zero in Eq. (13), the time evolution of the matrix $\hat{G}(\boldsymbol{k},t)$ is simply solved in the ω domain as

$$\hat{G}(\boldsymbol{k},\omega+i\eta) = \begin{bmatrix} \omega+i\eta-\epsilon_d(\boldsymbol{k})+\mu & -\epsilon\mathcal{J}_{\boldsymbol{k}}^* \\ -\epsilon\mathcal{J}_{\boldsymbol{k}} & \omega+i\eta+\epsilon_d(\boldsymbol{k})-\mu \end{bmatrix}^{-1}, \tag{24}$$

where a symmetry, $\epsilon(\boldsymbol{k}) = \epsilon(-\boldsymbol{k})$, is assumed.

When we follow the time evolution of $\hat{G}(\boldsymbol{k},t)$ under the influence of the mutual electron–electron interactions, there appear more complicated Green functions involving four or more operators, beyond the four components, $G_\uparrow$, $G_\downarrow$, $F_{\uparrow\downarrow}$, and $F_{\downarrow\uparrow}$. However, these complicated Green functions were shown to be deconvoluted into four Green functions and the two components of the self-energy.[9,48] Here, we assume that the thermodynamic limit has already been taken, and then we take the $\epsilon \to 0$ limit afterward.

To describe effects of many-body interactions in the superconducting phases, we will introduce the following two-component self-energy. Here, we assume a single orbital system and introduce the self-energy into the 2×2 matrix representation of the Green function as,

$$\hat{G}(\boldsymbol{k},\zeta) = \begin{bmatrix} \zeta+\mu-\epsilon_d(\boldsymbol{k})-\Sigma^{\rm nor}(\boldsymbol{k},\zeta) & -\Sigma^{\rm ano}(\boldsymbol{k},\zeta) \\ -\Sigma^{\rm ano}(\boldsymbol{k},\zeta) & \zeta-\mu+\epsilon_d(\boldsymbol{k})+\Sigma^{\rm nor}(\boldsymbol{k},-\zeta)^* \end{bmatrix}^{-1}, \tag{25}$$

where $\zeta = \omega + i\eta$, and two components, $\Sigma^{\rm nor}$ and $\Sigma^{\rm ano}$, represent normal and anomalous contributions of the self-energy, respectively.

While $[\hat{G}(\boldsymbol{k},\zeta)]_{11}$ represents a normal component of the matrix form of the Green function in Eq. (25) [the Green function for ↑-spin particle, $G_\uparrow(\boldsymbol{k},\zeta)$], $[\hat{G}(\boldsymbol{k},\zeta)]_{12}$ represents an anomalous component that emerges only when the system becomes superconducting [the anomalous Green function mixes ↑-spin particle and ↓-spin hole, $F_{\uparrow\downarrow}(\boldsymbol{k},\zeta)$]. The 11 element $[\hat{G}(\boldsymbol{k},\zeta)]_{11}$ has the same structure as,

$$[\hat{G}(\boldsymbol{k},\zeta)]_{11} = \frac{1}{\omega + i\eta + \mu - \epsilon_d(\boldsymbol{k}) - \Sigma^{\rm nor}(\boldsymbol{k},\omega) - W(\boldsymbol{k},\omega)}, \tag{26}$$

where the contribution from the anomalous component is give by

$$W(\boldsymbol{k},\omega) = \frac{\Sigma^{\rm ano}(\boldsymbol{k},\omega)^2}{\omega - \mu + \epsilon_d(\boldsymbol{k}) + \Sigma^{\rm nor}(\boldsymbol{k},-\omega)^*}. \tag{27}$$

The two components of the self-energy are rewritten as

$$\Sigma^{\rm nor}(\boldsymbol{k},\omega) = \frac{1}{\pi}\int d\omega' \frac{\mathcal{P}(\boldsymbol{k},\omega')}{\omega + i\eta - \omega'}, \tag{28}$$

$$\Sigma^{\rm ano}(\boldsymbol{k},\omega) = \frac{1}{\pi}\int d\omega' \frac{\mathcal{Q}(\boldsymbol{k},\omega') - \mathcal{Q}(\boldsymbol{k},-\omega')}{\omega + i\eta - \omega'}, \tag{29}$$

by introducing positive definite distributions, $\mathcal{P}(\boldsymbol{k},\omega)$ and $\mathcal{Q}(\boldsymbol{k},\omega)$. As discussed in the following sections, these distribution functions play pivotal roles.

While one-particle spectra are the focus of this article, there are other observables that can be utilized to study the many-body effects. Rather than the propagation of an electron or a hole excitation, the propagation of multiple electron and hole excitations are illustrated by many-particle Green functions, which are often useful in analyzing data from a range of spectroscopy (see Appendix A).

As a theoretical description of many-body quantum systems,[49] diagrammatic approaches have been developed,[50] in parallel to the variational wave-function approaches.[51–55] A formula for equilibrium free-energy given as a functional of the one-particle Green function has been formally constructed by a series expansion with respect to (screened/renormalized) interactions.[50] The series is terminated at a finite order[56,57] or the partial summation of a category of diagrams[58] is taken. A Monte Carlo sampling scheme based on the diagrams has also been developed.[59] While self-energy is a crucial building block in the diagrammatic approach, *vertex functions* are also vital to describe many-body effects.[31,60,61] The dynamical mean-field theory[62–65] and related non-perturbative approaches[66] have been developed. There are several extensions including vertex functions.[67] Two-particle Green functions have also been analyzed by extending the dynamical mean field theory.[68]

3. Methodology of Self-energy Analysis

To extract the self-energy from spectroscopy data, it is necessary to note that the measurements are conducted over a finite energy range, and that only the imaginary or real part of the Green functions is accessible in the data. When we analyze spectra and extract information of self-energy from these data, we need prior knowledge and a self-energy model, irrespective of their origin, to supplement the lack of the information. In standard theoretical approaches, the model has been often derived from first-principles formulae or approximated ones, as reviewed below.

3.1 Physics-informed self-energy model

3.1.1 Angle integrated

Local probes such as superconductor–normal-metal tunnel junction or scanning tunneling spectroscopy measurements capture the momentum integrated spectra or single-particle density of states,

$$N(\omega) = \int \frac{d^d k}{\Omega_{\rm BZ}} A(\boldsymbol{k},\omega), \tag{30}$$

where d is the dimension of the system. When we need to specify the phase in the following, we will add a subscript to N as $N_{\rm n}$ or $N_{\rm s}$, which correspond to the density of states in the normal and superconducting phase, respectively.

The density of states in strong-coupling Bardeen–Cooper–Schrieffer superconductors[69] have been well investigated by the Migdal–Eiashberg–Nambu theory.[47,70,71] Under certain conditions, the ratio of the density of states in the normal and superconducting phases is given by a simple function,[72,73]

$$\frac{N_{\rm s}(\omega)}{N_{\rm n}(\omega)} = {\rm Re}\left[\frac{\omega}{\sqrt{\omega^2 - \Delta(\omega)^2}}\right], \tag{31}$$

where $\Delta(\omega)$ is a gap function defined as

$$\Delta(\omega) = \frac{\Sigma^{\rm ano}(\omega)}{Z(\omega)}. \tag{32}$$

Here, $Z(\omega) = 1 - \Sigma^{\rm nor}(\omega)/\omega$ introduces renormalization of the effective mass.

The satisfactory condition to validate Eq. (31) is that $\epsilon(\boldsymbol{k})$ can be approximate as

$$\epsilon(\boldsymbol{k}) \simeq \mu + v_{\rm F}(|\boldsymbol{k}| - k_{\rm F}). \tag{33}$$

When the condition holds, the normal state density of state becomes constant as $N_{\rm n}(\omega) \propto 4\pi m_{\rm e} k_{\rm F}$.

We have prior knowledge that the superconducting gap $\Delta(\omega)$ will be formed in a small energy window in comparison with the Fermi energy $E_{\rm F}$ in the BCS superconductors. Thus, for ω significantly larger than a typical superconducting gap scale Δ_0, $N_{\rm s}(\omega)/N_{\rm n}(\omega)$ will approach unity. Then, we can access the entire ω dependence of the real part of $\omega/\sqrt{\omega^2 - \Delta(\omega)^2}$. By using the Kramers–Kronig relation, the imaginary part, thus, the whole complex function $\omega/\sqrt{\omega^2 - \Delta(\omega)^2}$ is obtained. Once the gap function $\Delta(\omega)$ is obtained from $N_{\rm s}(\omega)/N_{\rm n}(\omega)$ and the branch cut for $\sqrt{\omega^2 - \Delta(\omega)^2}$ is chosen, the normal and anomalous components of the self-energy will be analyzed.

The Migdal–Eliashberg–Nambu theory[70,71] provides us with simple formulae to model the two components, $\Delta(\omega)$ and $Z(\omega)$, by introducing an effective phonon density of states, $\alpha(\omega)^2 F(\omega)$ as explained in Appendix B. Then, the distributions, $\mathcal{P}(\boldsymbol{k},\omega)$ and $\mathcal{Q}(\boldsymbol{k},\omega)$, are obtained in a momentum-independent manner, as follows. The distribution $\mathcal{P}(\omega)$ is given by the following joint density of states of particle–hole and phonon excitations,

$$\mathcal{P}(\omega) = \pi\int_0^{+\infty} d\nu \frac{\alpha(\nu)^2}{N_{\rm n}(0)} F(\nu)[\theta(\omega-\nu)N_{\rm s}(\omega-\nu) + \theta(-\omega-\nu)N_{\rm s}(-\omega-\nu)] - \frac{1}{\pi}{\rm Im}\,\Sigma^{(0)}(\omega), \tag{34}$$

where the contribution from the self-energy $\Sigma^{(0)}(\omega)$ from impurity scattering and mutual electron–electron interactions. It is complicated to represent $\mathcal{Q}(\omega)$ by the densities of states, $\alpha(\nu)^2 F(\nu)$ and $N_{\rm s}(\omega)$. Instead, the distribution $\mathcal{Q}(\omega)$, which is not necessarily positive definite, is given by

$$\mathcal{Q}(\omega) = -\pi\int_0^{+\infty} d\nu \frac{\alpha(\nu)^2}{N_{\rm n}(0)} F(\nu) M_{\rm s}(\omega-\nu)$$

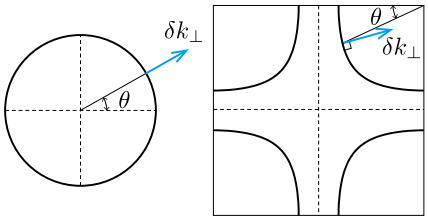

Fig. 2. (Color online) Fermi surface of two-dimensional electron gases and cuprates. While the left panel shows the Fermi surface, for the electron gas, the right panel shows the typical Fermi surface of the cuprate. In the both Fermi surfaces, a new coordinate, $(\delta k_\perp, \theta)$, used in the semi-angle dependent analysis, is illustrated.

$$\times \theta(\omega_c - \omega + \nu)\theta(\omega - \nu - \Delta_0), \tag{35}$$

where $M_s(\omega) = \mathrm{Re}[\Delta(\omega)/\sqrt{\omega^2 - \Delta(\omega)^2 + i\eta}]$.

References 74 and 75 made the formalism inverted the forward approach [Eqs. (B·1)–(B·3)] to extract $\alpha(\omega)^2 F(\omega)$. From the experimentally observed density of states for $eV_\ell \le \omega^{\mathrm{exp}} \le eV_h$, the self-energy is extracted by using the Migdal–Eliashberg–Nambu formalism, as summarized as follows:

$$N_s(\omega^{\mathrm{exp}})/N_n(\omega^{\mathrm{exp}})$$
$$\xrightarrow{\text{extrapolation}} N_s(\omega)/N_n(\omega)$$
$$\xrightarrow{\text{Eq. (31)}} \underbrace{\Delta(\omega) \overset{\text{Eqs. (B1)–(B3)}}{\underset{Z(\omega)}{\longleftrightarrow}} \alpha(\omega)^2 F(\omega)}_{\text{self-energy model}}$$

In Refs. 72 and 73, physically sound phonon density of states are assumed and examined whether these models explain experimentally observed tunneling spectroscopy data, while Refs. 74 and 75 inverted the procedure.

3.1.2 *Semi-angle resolved*

Vekhter and Varma extended the scheme developed in Refs. 72 and 73 to partially include momentum dependence of the self-energy.[76] A simple and useful example of the target systems is a two-dimensional many-body electrons. When we focus on the momentum near the Fermi surface, the momentum $\boldsymbol{k} = (k_x, k_y)$ in the Cartesian coordinate is rewritten into an angle along the Fermi surface, θ, and the momentum perpendicular to and measured from the Fermi surface, $\delta k_\perp$, as illustrated in Fig. 2.

Then, one may realize that the assumption of the linearized band dispersion Eq. (33) can be generalized as,

$$\epsilon(\boldsymbol{k}) \simeq \mu + v_F(\theta)\delta k_\perp. \tag{36}$$

The authors of Ref. 76 found that the density of states in Eq. (31) should be replaced with a partially integrated spectral function,

$$N(\theta, \omega) = \int d\delta k_\perp A(\delta k_\perp, \theta, \omega). \tag{37}$$

The ratio of the partially integrated spectral function satisfies a relation similar to Eq. (31) as,

$$\frac{N_s(\theta, \omega)}{N_n(\theta, \omega)} = \mathrm{Re}\left[\frac{\omega}{\sqrt{\omega^2 - \Delta(\theta, \omega)^2}}\right], \tag{38}$$

where $\Delta(\theta, \omega)$ is a partially momentum-dependent gap function.

3.1.3 *Angle-resolved*

Irrespective of perturbative[56–58] or non-perturbative,[66] theoretical and numerical methodologies have been developed to reveal the momentum-dependent structure of the self-energy. However, many of them are not simple and transferable enough to be utilized to extract self-energy information from experimental data.

Primarily focusing on the cuprates as a typical example of correlated quantum materials, there are analytical representations of the self-energy that capture the essence of cuprate physics. While the momentum-independent marginal-Fermi-liquid self-energy[77] has been employed in the literature, there have been several phenomenological self-energy models[78–82] to reproduce the significantly momentum-dependent nature of the self-energy of cuprate superconductors, which is evident in the formation of pseudogap.

The strongly momentum-dependent self-energy found in the two-dimensional Hubbard model by a cluster extension of the dynamical mean field theory[83] was reproduced by the dark fermion model,[80] in which hybridization between two species of fermions generates the pseudogap.[79,84] Such a singular self-energy has been found in fermion-boson coupled systems at quantum critical points.[81]

A completely different approach emerges from the AdS/CFT correspondence or holography.[85,86] A black hole in a anti-de Sitter spacetime offers a description of strange metals.[87,88] The strange metal shows $\delta k_\perp$-dependent the imaginary part of the self-energy proportional to $\omega^{2\nu_k}$ where ν_k is a linear function of $\delta k_\perp$, which is utilized in an analysis of ARPES measurements.[89]

3.2 *Machine-learning model*

Even though a physics-informed model or a decent approximation for the self-energy has succeeded in low-critical-temperature superconductors, it has a limitation and is often biased due to the physical mechanism behind the model. However, the accumulation of the studies on the self-energy has revealed its proper mathematical structures. If there are flexible mathematical representations for $\mathcal{P}$ and $\mathcal{Q}$, the proper mathematical structure and the prior knowledge will be exploited to construct a self-energy model beyond the limitation of these models.

3.2.1 *Artificial neural networks*

Artificial neural networks may serve as flexible models to represent these distributions, $\mathcal{P}$ and $\mathcal{Q}$. However, we note that there are several different structures of neural networks designed for different purposes. A typical category of artificial neural networks, widely used in recent machine- or deep-learning studies, is the feed-forward neural network. While a feed-forward neural network can represent (multivariate) distributions, as utilized in classification tasks, it is also suitable to use a feed-forward network to process the input vectors or matrices (pixel data).

A feed-forward neural network consists of successive transformations of a given input vector. For an $L^{(0)}$ dimensional input vector $\boldsymbol{x}^{(0)}$, a new $L^{(1)}$ dimensional vector $\boldsymbol{x}^{(1)}$ is generated through successive linear and non-linear transformation as, $x_\ell^{(1)} = \sigma^{(0)}(\sum_m W_{\ell m}^{(0)} x_m^{(0)} + b_\ell^{(0)})$. Here, $W^{(0)}$ is a $L^{(1)} \times L^{(0)}$ real matrix and $\boldsymbol{b}^{(0)}$ is a $L^{(0)}$ dimensional real vector, which are trainable parameters that define the linear

transformation of the input vector; the non-linear scalar function $\sigma^{(0)}(x)$ defines the non-linear transformation. We can repeat similar transformations as $x_\ell^{(k+1)} = \sigma^{(k)}(\sum_m W_{\ell m}^{(k)} x_m^{(k)} + b_\ell^{(k)})$ to construct a deep neural network. To train the neural network, we need to prepare a sizable set of input and output data.

There are several variants of feed-forward networks. A complex version of the feed-forward networks, where the parameters in $W^{(k)}$ and $\boldsymbol{b}^{(k)}$ are complex, is studied as an independent subject because the complex feed-forward neural networks show different analytical behavior. Convolutional neural networks, another variation of feed-forward networks, involve additional structured data operations, such as filtering and pooling, which are designed to handle images.

Another category of neural networks has been developed to represent, primarily, probability distributions, inspired by the Boltzmann weight, $e^{-\beta E(s)}/Z$, for a statistical description of classical many-body systems. Here, $E(\boldsymbol{s})$ is the energy of a given state represented by an array of Ising spins, $\boldsymbol{s}$, β is the inverse temperature, and Z is a normalization constant known as the partition function. While it is simple to sample a spin configuration $\boldsymbol{s}$ from the Boltzmann distribution, the full shape of the generated probability distribution is out of reach. One example in this category is the Boltzmann machine.[90,91] When an Ising spin configuration consists of a bit array $\boldsymbol{\sigma} = \{\sigma_\ell\}$ ($\sigma_\ell = 0, 1$) and a set of hidden variables $\boldsymbol{h} = \{h_m\}$ ($h_m = \pm 1$), a Boltzmann machine is given by a marginal probability $p(\boldsymbol{\sigma})$ through averaging a conditional probability $p(\boldsymbol{\sigma}|\boldsymbol{h}) = e^{-\beta E(\{2\sigma_\ell - 1\}, \{h_m\})}/Z$ over every possible configurations of the hidden variables. Depending on the interaction between the bit array $\boldsymbol{\sigma}$ and the hidden variables $\boldsymbol{h}$, there are several variations of the Boltzmann machines. While these Boltzmann machines have been used in a broad range of applications,[6,92] the author and the author's collaborators used them to represent the ω dependence of $\mathcal{P}(\boldsymbol{k}, \omega)$ and $\mathcal{Q}(\boldsymbol{k}, \omega)$ at a given $\boldsymbol{k}$.[93]

3.2.2 *Neural-network self-energy model*

As mentioned above, the Boltzmann machine, which originates from the Boltzmann weight for interacting Ising spins, returns a value associated with a bit array. To construct the Boltzmann machines to represent $\mathcal{P}$ and $\mathcal{Q}$, the authors mapped ω in a finite range, $\omega \in [-\Lambda/2, +\Lambda/2]$, to L-digit binary representation as

$$\boldsymbol{\sigma} \equiv (\sigma_0, \sigma_1, \ldots, \sigma_{L-1}), \tag{39}$$

by dividing the range $[-\Lambda/2, +\Lambda/2]$. Here, $\sigma_i = \mathrm{mod}(I/2^i, 2)$ for the decimal representation $I(\boldsymbol{\sigma})$ in the range $0 \leqq I(\boldsymbol{\sigma}) \leqq 2^L - 1$ of the grid number coordinate,

$$I(\boldsymbol{\sigma}) = \sum_{\ell=0}^{L-1} \sigma_\ell \cdot 2^\ell. \tag{40}$$

The binary representation introduces a hierarchical structure like a wavelet.[94,95] As shown below, the Boltzmann machines with parameters, whose number is proportional to a polynomial of L, can describe 2^L degrees of freedom. Similar structures of information compression have been utilized in matrix-product, tensor-network, or tensor-train representation.[96]

When ω dependence is discretized as above, the simplest choice of the basis set to describe $\mathcal{P}$ and $\mathcal{Q}$ is a rectangular function, $\Theta_{\boldsymbol{\sigma}}^L(\omega)$, defined as

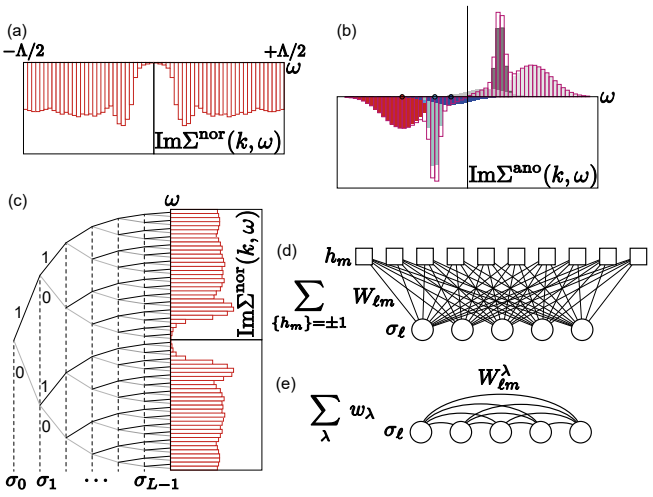

Fig. 3. (Color online) Boltzmann machine representation of self-energy. (a) The discretized representation of $\mathrm{Im}\,\Sigma^{\mathrm{nor}}(\boldsymbol{k}, \omega) = -\mathcal{P}(\boldsymbol{k}, \omega)$ is illustrated as a combination of red rectangles. (b) The discretized mixture representation of $\mathrm{Im}\,\Sigma^{\mathrm{ano}}(\boldsymbol{k}, \omega) = \mathcal{Q}(\boldsymbol{k}, \omega) - \mathcal{Q}(\boldsymbol{k}, -\omega)$ is shown. Whereas the total mixture distribution for $\mathcal{Q}(\boldsymbol{k}, \omega)$ is represented by open red rectangles, each Boltzmann-machine distribution is illustrated by filled red, cyan, and blue rectangles. Copies of Boltzmann machines, $-\mathcal{Q}(\boldsymbol{k}, -\omega)$, are shown in grey rectangles. (c) The wavelet-like structure of the rectangular basis set is illustrated. From the longest wave length structure governed by σ_0 to the shortest wave length structure controlled by σ_{L-1}, each rectangular basis (open red rectangle) is labeled by the set of bits $\boldsymbol{\sigma} = (\sigma_0, \sigma_1, \ldots, \sigma_{L-1})$ ($\sigma_\ell = 0, 1$). The structure of the restricted Boltzmann machine for $C(\boldsymbol{\sigma})$ and mixture distribution consisting of Boltzmann machines for $D(\boldsymbol{\sigma})$ is depicted in (d) and (e), respectively. This figure is taken from Ref. 93 under the terms of the Creative Commons Attribution 4.0 International license.

$$\Theta_{\boldsymbol{\sigma}}^L(\omega) = \begin{cases} 1 & \text{for } x \in [I(\boldsymbol{\sigma})/2^L, [1 + I(\boldsymbol{\sigma})]/2^L) \\ 0 & \text{otherwise} \end{cases}. \tag{41}$$

The discretized description of the self-energy is shown in Fig. 3. The rectangular function is also convenient to calculate the self-energy since the Kramers–Kronig transformation of $\Theta_{\boldsymbol{\sigma}}^L(\omega)$ is analytically available.

Then, the basis set expansions of $\mathcal{P}(\boldsymbol{k}, \omega)$ and $\mathcal{Q}(\boldsymbol{k}, \omega)$, at a given $\boldsymbol{k}$, are obtained as

$$\mathcal{P}(\boldsymbol{k}, \omega) = \sum_{\boldsymbol{\sigma}} C_{\boldsymbol{k}}(\boldsymbol{\sigma}) \Theta_{\boldsymbol{\sigma}}^L\left(\frac{\omega + \Lambda/2}{\Lambda}\right), \tag{42}$$

$$\mathcal{Q}(\boldsymbol{k}, \omega) - \mathcal{Q}(\boldsymbol{k}, -\omega) = \sum_{\boldsymbol{\sigma}} D_{\boldsymbol{k}}(\boldsymbol{\sigma}) \left[\Theta_{\boldsymbol{\sigma}}^L\left(\frac{\omega + \Lambda/2}{\Lambda}\right) - \Theta_{\boldsymbol{\sigma}}^L\left(\frac{\Lambda/2 - \omega}{\Lambda}\right)\right], \tag{43}$$

with two functions, $C_{\boldsymbol{k}}(\boldsymbol{\sigma})$ and $D_{\boldsymbol{k}}(\boldsymbol{\sigma})$. Below, the momentum index $\boldsymbol{k}$ is omitted for simplicity, and $C_{\boldsymbol{k}}(\boldsymbol{\sigma})$ and $D_{\boldsymbol{k}}(\boldsymbol{\sigma})$ are denoted as $C(\boldsymbol{\sigma})$ and $D(\boldsymbol{\sigma})$, respectively.

Due to the non-negativity of $C(\boldsymbol{\sigma})$, it is efficiently represented by the restricted Boltzmann machine (RBM),[91,97,98] as

$$\mathcal{C}(\boldsymbol{\sigma}) = e^b \sum_{\{h_m\}=\pm 1} \exp\left[\sum_{\ell,m} (2\sigma_\ell - 1) W_{\ell m} h_m\right] = e^b \prod_{m=0}^{L_{\mathrm{h}}-1} 2\cosh\left[\sum_{\ell} (2\sigma_\ell - 1) W_{\ell m}\right], \tag{44}$$

where L_{h} is the number of the hidden variables, b is the bias, and the weight $W_{\ell m}$ only connects a visible variable σ_ℓ and a

hidden variable h_m, as illustrated in Fig. 3(d). The advantage of the RBM is that one can analytically trace out the hidden variables h_m, leading to the second line in the above formula.

The normal component and anomalous component of the self-energy could be influenced by different physical processes in different energy scales. While $\mathcal{P}(\omega)$ could be significant up to several eV scale, $\mathcal{Q}(\omega)$ would be finite within a smaller energy scale. To introduce prior knowledge on the energy scale, it is convenient to represent $D(\boldsymbol{\sigma})$ by a localized distribution. In Ref. 93, the authors introduced a linear combination of the simple Boltzmann machine without hidden variables [see Fig. 3(e)] as

$$D(\boldsymbol{\sigma}) = \sum_{\lambda} w_{\lambda} \exp\left[\sum_{\ell}(2\sigma_{\ell}-1)b_{\ell}^{\lambda} + \sum_{\ell,m}(2\sigma_{\ell}-1)W_{\ell m}^{\lambda}(2\sigma_{m}-1)\right], \tag{45}$$

where a linear combination of the Boltzmann machines are taken with coefficients, $\{w_{\lambda}\}$. The coefficients, the biases, $\{b_{\ell}^{\lambda}\}$, and the weights, $\{W_{\ell m}^{\lambda}\}$, will be optimized.

Note that a linear combination of Gaussian distributions is one of the standard procedures to approximate a smooth function[99] and can be used as an initial guess of $D(\boldsymbol{\sigma})$ (the detailed procedure is given in Appendix of Ref. 93).

While the restricted Boltzmann machine with enough number of hidden variables can represent any positive definite distribution,[100,101] it is not easy to initialize the restricted Boltzmann machines. In contrast, the Boltzmann machines without the hidden variables are explicitly initialized to represent several distributions, including Gaussian distributions. To reconcile the drawbacks and benefits of the Boltzmann machine, the authors of Ref. 93 choose a linear combination of the Boltzmann machines for the anomalous part.

3.2.3 *Training of Boltzmann-machine models*

Reference 93 introduces a training procedure for these (restricted) Boltzmann machines, which consists of inner and outer loops (as later illustrated in Fig. 4). The mean squared error between the experimental and theoretical spectrum is minimized as the cost function in the inner loop. The cost function is defined as,

$$\chi^2(\boldsymbol{k}) = \frac{1}{N_{\mathrm{d}}}\sum_{j}[A^{\mathrm{exp}}(\boldsymbol{k},\omega_j) - A^{\mathrm{cal}}(\boldsymbol{k},\omega_j)]^2, \tag{46}$$

where the photoelectron intensity is measured or calculated at N_{d} discrete energy points $\{\omega_j\}$. Here, the experimental spectrum is denoted by $A^{\mathrm{exp}}(\boldsymbol{k},\omega)$ while the theoretical spectrum, obtained by the Boltzmann-machine self-energy models, is denoted by $A^{\mathrm{cal}}(\boldsymbol{k},\omega)$, where $A^{\mathrm{cal}}(\boldsymbol{k},\omega)$ is a product of a Fermi-Dirac distribution $f_{\mathrm{FD}}(\omega)$ (convoluted with a Lorentzian representing an experimental resolution) and the spectral function $A(\boldsymbol{k},\omega)$. To minimize χ^2, the variational parameters,

$$\boldsymbol{\alpha}^C = (b, \{W_{\ell m}\})^T \tag{47}$$

and

$$\boldsymbol{\alpha}^D = (\{w_{\lambda}\}, \{b_{\ell}^{\lambda}\}, \{W_{\ell m}^{\lambda}\})^T, \tag{48}$$

in $C(\boldsymbol{\sigma})$ and $D(\boldsymbol{\sigma})$, are optimized by using the gradients,

$$\boldsymbol{g}^{C,D} = \frac{\partial \chi^2}{\partial \boldsymbol{\alpha}^{C,D}}. \tag{49}$$

The increments of these parameters, $\delta\boldsymbol{\alpha}^C$ and $\delta\boldsymbol{\alpha}^D$, are chosen to be

$$\delta\boldsymbol{\alpha}^C = -\frac{\epsilon^C}{\|S^{-1}\boldsymbol{g}^C\|^p} S^{-1}\boldsymbol{g}^C, \tag{50}$$

$$\delta\boldsymbol{\alpha}^D = -\frac{\epsilon^D}{\|\boldsymbol{g}^D\|^p} \boldsymbol{g}^D, \tag{51}$$

where $\epsilon^{C,D}$ are the learning rates and a real number, $p \in (0,1)$, controls the amplitude of the gradient. While the mixture of the Boltzmann machines, $D(\boldsymbol{\sigma})$, will be updated in the outer loop as well, the restricted Boltzmann machine $C(\boldsymbol{\sigma})$ is updated only in the inner loop. Then, the natural gradient method is used to update $\boldsymbol{\alpha}^C$ in Ref. 93. The increment of $\boldsymbol{\alpha}^C$ involves the classical Fisher information matrix given by,

$$S_{\mu\nu} = \sum_{j} \frac{\partial \mathcal{P}(\omega_j)}{\partial \alpha_{\mu}^C} \frac{\partial \mathcal{P}(\omega_j)}{\partial \alpha_{\nu}^C}. \tag{52}$$

The outer loop then examines the test error defined as,

$$\widetilde{\chi}^2(\boldsymbol{k}) = \frac{1}{N_{\mathrm{syn}}N_{\mathrm{d}}}\sum_{j,k}[A_k^{\mathrm{syn}}(\boldsymbol{k},\omega_j) - A^{\mathrm{cal}}(\boldsymbol{k},\omega_j)]^2, \tag{53}$$

where a set of N_{syn} synthetic spectra, $\{A_k^{\mathrm{syn}}(\boldsymbol{k},\omega_j)\}$, is used to avoid overfitting.[93]

3.3 *Workflow*

Along with the workflow for the forward approach[72,73] according to the Migdal–Eliashberg–Nambu theory, the workflows for the self-energy estimation utilizing the physics-informed models[74–76] (in Sects. 3.1.1 and 3.1.2) and the Boltzmann-machine models (in Sect. 3.2), are summarized in Fig. 4.

4. Self-energy Analysis of Experimental Data

4.1 *Normal state*

While understanding strong-coupling BCS superconductivity was an important subject in an early stage of the self-energy analysis, the self-energy in the normal states have been studied in variety of materials. The mutual Coulomb repulsion and the electron–phonon coupling will make a considerable impact on the quasiparticle spectra even in the normal metallic states. For example, strong ω dependence of $\mathrm{Re}\,\Sigma(\omega)$ in the electron–phonon coupled systems[103–105] has been shown to generate a bend in electronic dispersion, which is often called a kink. Due to development of non-perturbative theoretical analyses of the self-energy, it has been theoretically revealed that the Coulomb repulsion itself generate the kink structure,[106–108] as well. The kink structures have been intensively discussed in the cuprate superconductors, where the Coulomb repulsion plays an important role. It is highly desirable to understand the complicated kink anomalies found in the quasiparticle dispersion of the cuprates.[109]

4.1.1 *Surface state of Be(0001)*

Analysis of self-energy in a simple system is favorable to understand the nature of electron–phonon couplings and electron–electron interactions. A many-body electron system

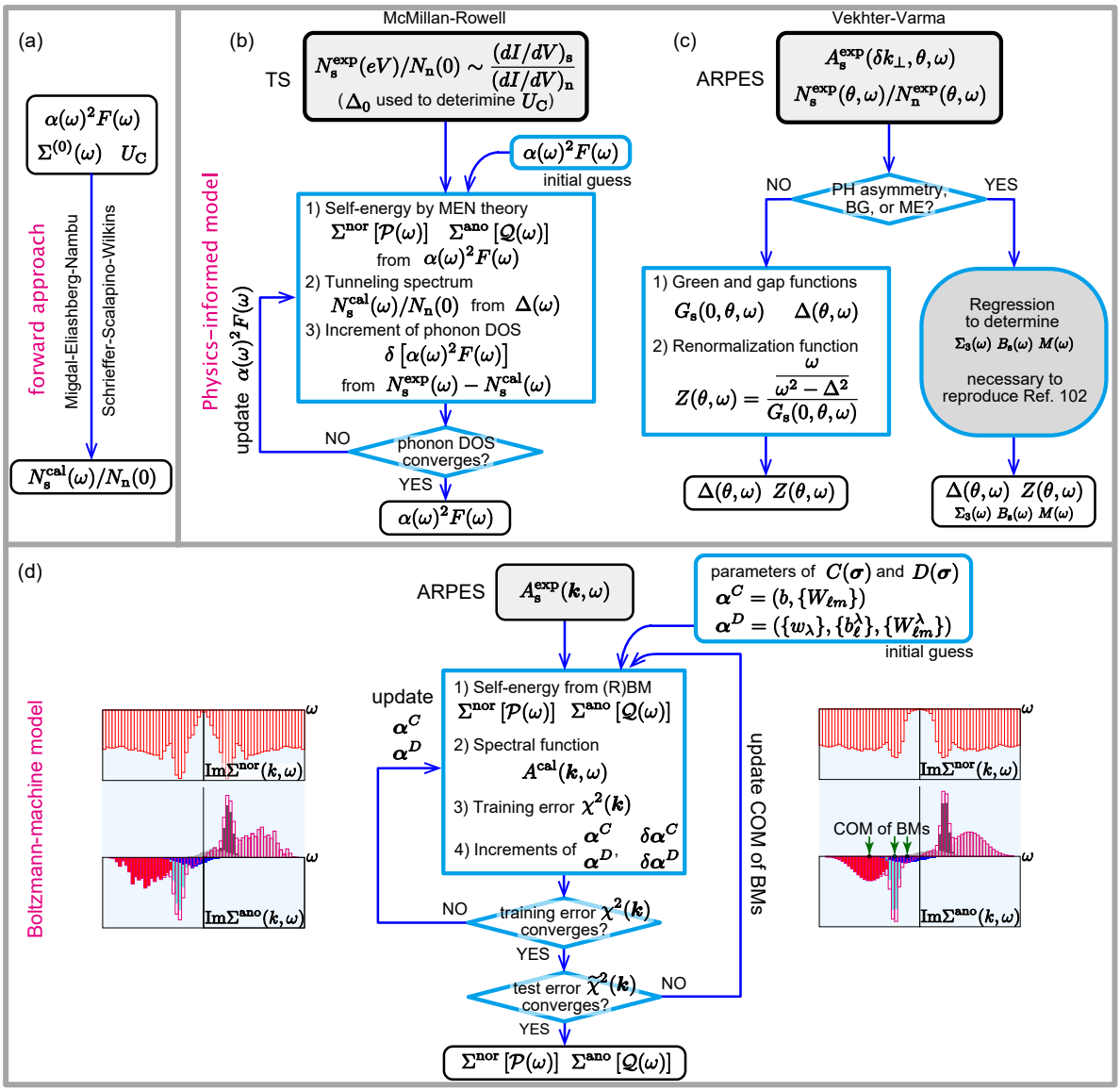

Fig. 4. (Color online) Workflows for forward and inverted approaches. (a) The Migdal–Eliashberg–Nambu (MEN) theory and the Scrieffer–Scalapino–Wilkins scheme provide a forward approach to calculate tunneling spectra (TS), $N_s^{cal}(\omega)/N_n(0)$, by assuming an effective boson density of states (DOS), $\alpha(\omega)^2F(\omega)$, the self-energy, $\Sigma^{(0)}(\omega)$, induced by electron–electron interaction, and the Coulomb pseudopotential, U_C (see Appendix B). (b) The McMillan–Rowell method partially inverts the forward approach to obtain the effective phonon density of states, $\alpha(\omega)^2F(\omega)$, from the experimentally observed tunneling spectrum, $N_s^{exp}(\omega)/N_n(0)$, supplemented by Δ_0 from the spectrum. (c) The inverted scheme is further extended in the Vekhter–Varma method, where the ARPES spectra is utilized to estimate the self-energy. Reference 102 generalizes the method by incorporating the particle–hole (PH) asymmetric component of self-energy, $\Sigma_3(\theta,\omega)$, with separating so-called backgrounds (BG), $B_s(\delta k_\perp,\theta,\omega)$, and matrix elements (ME), $M(\theta,\omega)$, from bare photoemission spectra. (d) Workflow represents a regression procedure to train the Boltzmann-machine self-energy models, proposed in Ref. 93. The parameters, $\boldsymbol{\alpha}^C$ and $\boldsymbol{\alpha}^D$, in $C(\boldsymbol{\sigma})$ and $D(\boldsymbol{\sigma})$ are updated by the inner and outer loops.

with spherically-symmetric quadratic band dispersion will serve as such a reference. While the simplest example would be a two-dimensional electron gas emerging in semiconductor interfaces, the photoemission spectroscopy of the interfaces is not simple.[110] Instead, the surface states of metals have been studied.[111–114] One of these studies was performed on the Be(0001) surface.[115]

The authors of Ref. 115 performed a *forward* analysis on the ARPES spectra of the Be(0001) surface. They introduced the self-energy Σ^{ph} modeling the electron–phonon couplings and compared the spectral weight generated by Σ^{ph} and the effects of the electron–electron interaction. Here, Σ^{ph} is estimated by using the Migdal–Eliashberg formalism in the normal state.

The authors approximated $\alpha(\omega)^2F(\omega)$ as

$$\alpha(\omega)^2F(\omega) = \lambda\omega\theta(\omega_{ph}-\omega)/2\omega_{ph},$$

where λ is the strength of the electron–phonon coupling and ω_{ph} is the maximum energy scale of the phonon measured by electron-energy loss spectroscopy.[116] Here, the distribution function is given as

$$\mathcal{P}(\omega) = \pi\theta(\omega_{ph}-|\omega|)\lambda\omega^2/4\omega_{ph} + \pi\theta(|\omega|-\omega_{ph})\lambda\omega_{ph}/4,$$

which is an example of the self-energy model for the two-dimensional electron–phonon coupled systems.

The electron–phonon coupling strength λ is estimated from the ratio of the renormalized electron velocity v_F^* and bare velocity v_F through $1+\lambda = v_F/v_F^*$. These velocities are

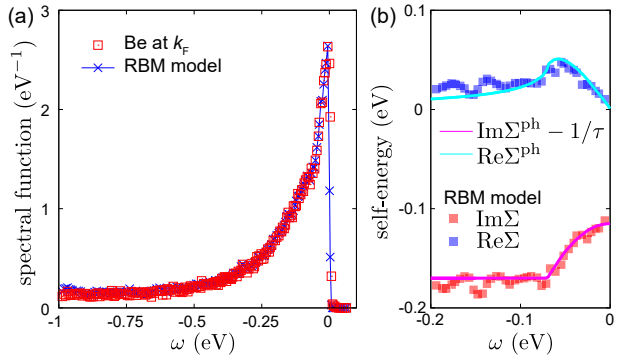

Fig. 5. (Color online) Self-energy models for Be(0001) surface state. The left panel shows the ARPES spectrum at the Fermi momentum k_F (red open squares) with the spectral function generated by the RBM self-energy model (blue crosses). The right panel illustrates the self-energy models. Here, the Migdal–Eliashberg self-energy model represented by solid curves shows the imaginary part of Σ^{ph} as a piecewise function of ω. While the impurity scattering term $-1/\tau$ is introduced, the small pseudoparabolic term in Ref. 115 is neglected. For $|\omega| < \omega_{\mathrm{ph}}$, $\mathrm{Im}\,\Sigma^{\mathrm{ph}}$ is proportional to ω^2 while $\mathrm{Im}\,\Sigma^{\mathrm{ph}}$ is constant for $|\omega| > \omega_{\mathrm{ph}}$. A peak in $\mathrm{Re}\,\Sigma^{\mathrm{ph}}$ for $|\omega| \lesssim \omega_{\mathrm{ph}}$ generates a kink in the quasiparticle dispersion. The RBM self-energy model (blue and red filled squares) is consistent with the Migdal–Eliashberg self-energy model.

estimated from the dispersion measured by the angle-resolved photoemission[117] as $\epsilon(\boldsymbol{k}) \simeq v_{\mathrm{F}}^*(|\boldsymbol{k}| - k_{\mathrm{F}})$ for $-\omega_{\mathrm{ph}} \lesssim \omega$ and $\epsilon(\boldsymbol{k}) \simeq v_{\mathrm{F}}(|\boldsymbol{k}| - k_{\mathrm{F}})$ for $\omega \ll -\omega_{\mathrm{ph}}$. The transition from v_{F}^* to v_{F} is observed as a kink in the band dispersion.

So far, the self-energy model is determined through experiments other than the ARPES measurement. The authors also introduced a pseudoparabolic electron–electron self-energy and impurity scattering as fitting parameters to reproduce the ARPES spectra of the Be(0001) surface state.

While the authors of Ref. 115 utilized several independent experimental data to obtain a decent self-energy model, the RBM representation is capable to obtain the self-energy by using a single ω dependence of the spectrum at a given momentum. As shown in Fig. 5, the self-energy obtained by the RBM is consistent with the self-energy model in Ref. 115 even though there are noise in the RBM self-energy model due to statistical errors in the ARPES measurement.

4.1.2 $SrVO_3$

Another example is a perovskite vanadium oxide $SrVO_3$, whose spectrum has been experimentally and theoretically studied as a typical correlated metal.[106,118–121] By assuming that the (retarded) self-energy satisfies a particle–hole symmetry and supplementing high-energy tails of the spectral function, the normal-state self-energy of $SrVO_3$ is extracted from the ARPES data.[120]

Photoemission spectroscopy mainly provides us with information regarding occupied states, though unoccupied states above the Fermi energy can be partially observed at finite temperatures[122–124] or through pump-probe measurements.[125,126] Therefore, we need to extract the self-energy from a spectrum within a finite range of binding energy observed as $A(\boldsymbol{k}, \omega_{\mathrm{exp}})$ for $-\omega_{\mathrm{c}} \le \omega^{\mathrm{exp}} \lesssim 0$.

By assuming the particle–hole symmetry and high-energy tails of the spectrum, and the particle–hole symmetry of the self-energy as $\Sigma(-\boldsymbol{k}, -\omega) = -\Sigma(\boldsymbol{k}, \omega)^*$, the authors obtained the self-energy, as follows. From these assumption, the authors constructed the spectral function $A(\boldsymbol{k}, \omega)$ practically along the entire ω axis. The retarded Green function is then obtained through the Hilbert transformation (or the Kramers–Kronig relation)

$$G(\boldsymbol{k}, \omega) = \int_{-\infty}^{+\infty} \frac{A(\boldsymbol{k}, \omega')}{\omega + i\eta - \omega'}\, d\omega'. \tag{54}$$

The inverse of $G(\boldsymbol{k}, \omega)$ provides us with $\epsilon(\boldsymbol{k}) - \mu + \Sigma^{\mathrm{nor}}(\boldsymbol{k}, \omega)$. The extracted self-energy is qualitatively consistent with the results of a numerical simulation.[106]

When these assumptions hold, the normal-state self-energy is reproduced through the above scheme. If the assumption concerning the high-energy tails is not reliable, regression will be more suitable for extracting the self-energy. When we wish to analyze superconductors, the present scheme provides only the total self-energy, $\Sigma^{\mathrm{nor}}(\omega) + W(\omega)$. Thus, a regression scheme based on a flexible self-energy model will be useful for analyzing the superconducting states.

4.1.3 Cuprate

The normal-state self-energy in a cuprate superconductor was also analyzed by assuming fermion-boson coupling mechanism.[109] Here, the dispersion along the nodal direction $\theta \sim \pi/4$ was studied.

When the momentum dependence of $\Sigma(\boldsymbol{k}, \omega)$ along the nodal direction is negligible, the spectral function is given by

$$-\frac{1}{\pi} \frac{\mathrm{Im}\,\Sigma(\omega)}{[\omega + \mu - \epsilon(\boldsymbol{k}) - \mathrm{Re}\,\Sigma(\omega)]^2 + \mathrm{Im}\,\Sigma(\omega)^2}.$$

If the amplitude of the self-energy is smaller than or comparable with the bare dispersion, the maximum of the spectral function appears along $\omega + \mu - \epsilon(\boldsymbol{k}) - \mathrm{Re}\,\Sigma(\omega) = 0$.

Therefore, by assuming a bare band dispersion $\epsilon(\boldsymbol{k})$, the real part of the self-energy is estimated from the positions of the peaks of the spectra in $\boldsymbol{k}, \omega$ space, where the peak of the spectrum is determined by the momentum distribution curves method. By assuming the Migdal–Eliashberg formalism, the bosonic density of states was inferred from the obtained real part of the self-energy.[109] However, the momentum dependence of the self-energy along the nodal direction has been examined in details and found to be non-negligible.[89]

4.2 Superconducting state

4.2.1 Pb

The self-energy analysis by combining the Migdal–Eliashberg–Nambu theory, Eq. (31), and the tunneling spectra, has succeeded to demonstrate the validity of the phonon mechanism for the low-temperature BCS superconductors, while it sacrifices many-body effects inherent in the normal state by assuming the normal state with constant density of states. Even though the theoretical framework thoroughly depends on the phonon mechanism and the normal-state density of states often shows anomalies, $\alpha(\omega)^2F(\omega)$ behind $\mathcal{P}(\omega)$ and $\mathcal{Q}(\omega)$ is the extracted.

While the phonon density of states is approximated by two Lorentzian distributions in Ref. 72, $\alpha(\omega)^2F(\omega)$ is iteratively updated starting from an initial guess to minimize the difference between the tunneling spectrum given by the current $\alpha(\omega)^2F(\omega)$ and that obtained in the tunneling experiment of Pb, in Ref. 74. Finally, the authors of

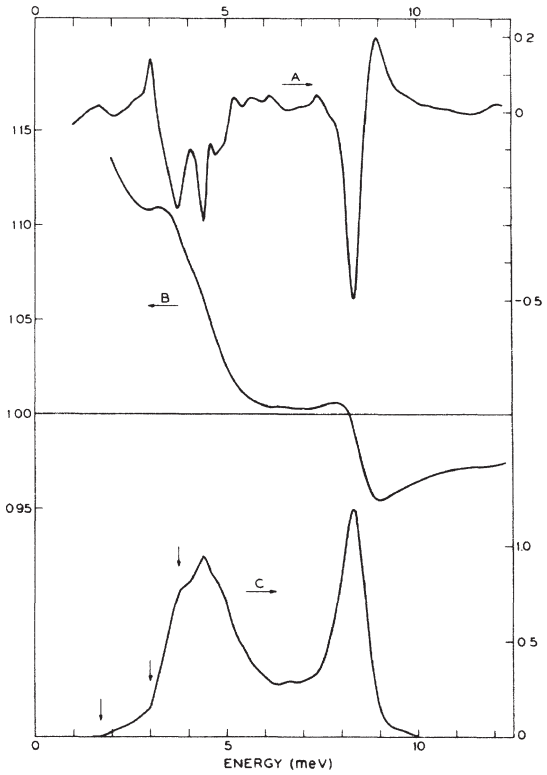

Fig. 6. Analysis of tunneling spectrum of Pb. Curve A represents the voltage derivative of the ratio of tunneling conductance in the superconducting state and normal state, in units meV^{-1} as a function of $V - 2\Delta_0$, where Δ_0 is defined in Appendix B. Curve B is $N_s(\omega)/N_n(\omega)$ as a function of $\omega - \Delta_0$ while Curve C is the dimensionless phonon density of states, $\alpha(\omega)^2F(\omega)$, as a function of ω. Reprinted figure with permission from Ref. 74. © 1965 American Physical Society.

Ref. 74 obtained $\alpha(\omega)^2F(\omega)$ from the tunneling spectrum of Pb, as shown in the bottom panel of Fig. 6.

The detailed structures in the density of states $N(\omega)$ of Pb by superconductor-insulator-normal tunnelings[128] is also observed by angle-integrated photoemission spectroscopy measurements.[129]

4.2.2 *Sn and others*

By using the same formalism, the phonon density of states of β-Sn or white tin has been studied[75] as a weaker coupling system. The extracted phonon density of states is quantitatively consistent with the phonon dispersion observed in inelastic neutron scatterings.[130,131] Other examples of similar analyses are found in an extensive review article.[132]

4.2.3 *Cuprate*

While the total self-energy of the cuprates has been known for more than two decades,[133] the decomposition of the normal and anomalous components of the self-energy was performed within a decade. Bok et al. applied the extension of the Migdal–Eliashberg–Nambu theory[76] to the ARPES spectra around the nodal direction.[102] The validity of the self-energy analysis is limited by the usage of Eq. (31), which is hardly justified around the antinodal region ($\theta \sim 0$ in Fig. 2). Later, Li et al. introduced phenomenological self-energy models to analyze the entire Brillouin zone of the cuprate,[134] where the distribution function for the anomalous component, $Q(\omega)$, is assumed to be finite in an extended energy scale. To remove constraints on these self-energy models, the Boltzmann machines were used to represent $\mathcal{P}$ and $\mathcal{Q}$[93] as reviewed in Sect. 3.2.

At a given momentum around the antinodal region, which is a Fermi momentum at higher temperatures than T_c, the self-energy was extracted from the energy dependence of the ARPES spectrum of a category of cuprates. As shown in Fig. 7, the prominent peak structures in $\mathcal{Q}$ and $\mathrm{Im}\,\Sigma^{\mathrm{ano}}$, which generate a significant superconducting gap, is compensated by the peak structures in $\mathrm{Im}\,W$. Then, the total self-energy does not show such prominent anomalies.

The compensation of the peak structures in the self-energy is an unexpected from the phonon mechanism, which sets a constraint on the mechanism of the high-temperature superconductivity of the cuprates. In addition, it is revealed that the incoherence of the one-particle excitations, quantitatively estimated from the self-energy, enhances the superconducting critical temperatures,[93] which is seemingly counterintuitive.

5. Summary and Future Perspectives

To understand effects of mutual interactions in quantum many-body systems, self-energy is an important physical quantity, which is unfortunately not an observable in experiments. The self-energy has been indeed crucial to theoretically understand the origin of the strong-coupling Bardeen–Cooper–Schrieffer (BCS) superconductivity. By solving inverse problems formulated with a sophisticated many-body perturbation theory, the self-energy was extracted from spectroscopy data of Pb and other strong coupling BCS superconductors.

Alongside the development of theoretical tools and spectroscopy measurements, the rise of machine learning has inspired researchers to formulate the inverse problem from a broader perspective. While there are various machine-learning-inspired approaches to analysis of spectroscopy data, we focused on photoemission spectroscopy measurements and reviewed the self-energy analysis by using the Boltzmann machine.

The self-energy analysis of superconductors is distilled to optimization of two distribution functions, $\mathcal{P}(\boldsymbol{k}, \omega)$ and $\mathcal{Q}(\boldsymbol{k}, \omega)$, which generate the normal and superconducting components of the self-energy through a transformation [Eqs. (28) and (29)]. Then, we can employ various description of $\mathcal{P}(\boldsymbol{k}, \omega)$ and $\mathcal{Q}(\boldsymbol{k}, \omega)$. The machine learning approaches provide us with a variety of models for complicated probability distributions and, thus, a flexible description of the self-energy. As an example of these approaches, the Boltzmann machine representation of the self-energy and its application to the copper oxide high-temperature superconductors are reviewed in the present article.

Even though the machine learning approaches are flexible, there remain several crucial problems. While the Boltzmann machines are simple and sallow neural networks, the optimization is not straightforward. The limitation of available experimental data also remains a crucial problem. While spectra in a wide energy range are available, momentum dependence is not accessible in the tunneling spectroscopy. In contrast, the angle-resolved photoemission spectroscopy (ARPES) provides us with momentum dependence of one-particle spectra while only spectra for ω smaller than the Fermi level are available. The validation of

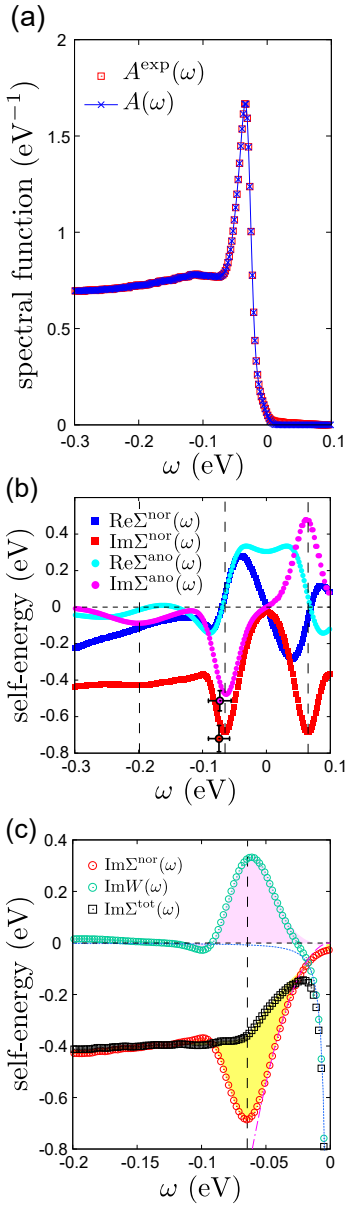

Fig. 7. (Color online) Self-energy of a cuprate represented by the Boltzmann machines.[93] (a) An experimental ARPES spectrum $A^{\rm exp}(\omega)$ of $Bi_2Sr_2CaCuO_{8+\delta}$ ($T_c = 90$ K) at a Fermi momentum (red open squares)[127] is compared with the spectral function given by the Boltzmann-machine self-energy shown in (b). (b) The real and imaginary parts of normal and anomalous components of the self-energy are shown. (c) The total self-energy is decomposed into the normal component and W, where the peak structure in the normal component is compensated by the peak in Im $W(\omega)$.

the obtained self-energy remains an important issue as well. Though efforts have been made to validate the self-energy obtained from the spectroscopy data (as in Appendix of Ref. 93), there could be local minima in the optimization problems, due to the lack of information.

Therefore, we need to explore further possibilities to augment the machine-learning approaches. A possible approach will be utilization of other experimental data or simulations as prior knowledge. The momentum dependence could be extracted from interference in scanning tunneling microscope[135–139] although it requires theoretical tools. To supplement the photoemission spectra, inverse photoemission would be useful, though the resolution of the inverse photoemission is lower than the photoemission so far. Combined one- and two-particle excitations observed in resonant inelastic x-ray scattering[140–142] will provide us with further information.

Acknowledgments The author thanks Teppei Yoshida, Atsushi Fujimori, and Masatoshi Imada for collaboration and ongoing discussions on spectroscopy. The author also thanks Shiro Sakai, Takeshi Kondo, Yuhki Kohsaka, and Tetsuo Hanaguri for insightful discussions. The numerical data shown in Fig. 1 was obtained by an in-house extension of mVMC[143] developed by Maxime Charlebois, which is detailed in Ref. 32. We acknowledge the financial support of JSPS Kakenhi Grant No. 23H04524. This work used computational resources of supercomputer Fugaku provided by R-CCS through the HPCI System Research Project (Project ID: hp230169). This study was also supported by MEXT as a program for promoting researches on the supercomputer Fugaku [AI Numerical Spectroscopy for Analyzing Emergent Structures of Quantum Entanglement in Correlated Quantum Materials (JPMXP1020230410)] and used computational resources of supercomputer Fugaku provided by R-CCS (Project ID: hp230213). MANA is supported by World Premier International Research Center Initiative (WPI), MEXT, Japan.

Appendix A: Two-particle Green Functions

A typical example of two-particle Green functions is a dynamical spin susceptibility defined as

$$\chi^{zz}(\boldsymbol{q},\omega) = \langle\Phi_0|\hat{S}^z(\boldsymbol{q})^\dagger \frac{1}{\omega + i\eta - \hat{H} + E_0}\hat{S}^z(\boldsymbol{q})|\Phi_0\rangle,$$

which describes spin excitations generated by operating a spin operator,

$$\hat{S}^z(\boldsymbol{q}) = (1/2)\sum_{\boldsymbol{k}}(\hat{c}^\dagger_{\boldsymbol{k}+\boldsymbol{q}\uparrow}\hat{c}_{\boldsymbol{k}\uparrow} - \hat{c}^\dagger_{\boldsymbol{k}+\boldsymbol{q}\downarrow}\hat{c}_{\boldsymbol{k}\downarrow}),$$

to the ground state $|\Phi_0\rangle$. Similarly to the one-particle Green functions, the imaginary part of the dynamical susceptibility provides dynamical structure factor as,

$$S^{zz}(\boldsymbol{q},\omega) = -\frac{1}{\pi}\mathrm{Im}\,\chi^{zz}(\boldsymbol{q},\omega).$$

To extract a two-particle self-energy, we need to introduce a proper *single-particle* dispersion as a reference. The single-particle dispersion will be given by a dispersion relation of, for example, magnons[144] or triplons.[145] Even in the simple Heisenberg model on a square lattice, the self-energy is evident as deviation from the magnon dispersion obtained by the linear spin wave theory.[146]

Appendix B: Migdal–Eliashberg–Nambu Theory

The Migdal–Eliashberg–Nambu theory[47,70,71] provides us simple formulae to model the two components, $\Delta(\omega)$ and $Z(\omega)$, by introducing an effective phonon density of states, $\alpha(\omega)^2F(\omega)$ as explained below. The normal and anomalous components of the self-energy are given by

$$\Sigma^{\rm nor}(\omega) = [1 - Z(\omega)]\omega = \int_{\Delta_0}^{\infty} d\omega'\,\mathrm{Re}\left[\frac{\omega'}{\sqrt{\omega'^2 - \Delta(\omega')^2 + i\eta}}\right]K_-(\omega,\omega') + \Sigma^{(0)}(\omega), \quad (B\cdot1)$$

$$\Sigma^{\rm ano}(\omega) = Z(\omega)\Delta(\omega) = \int_{\Delta_0}^{\omega_c} d\omega'\,\mathrm{Re}\left[\frac{\Delta(\omega')}{\sqrt{\omega'^2 - \Delta(\omega')^2 + i\eta}}\right][K_+(\omega,\omega') - N_{\rm n}(0)U_{\rm C}], \quad (B\cdot2)$$

where $\Delta_0 = \mathrm{Re}\,\Delta(\Delta_0)$, ω_c is the cutoff frequency, $N_n(0)U_C$ is a Coulomb pseudopotential,[147,148] and η is a positive broadening factor. Here, the kernel functions $K_\pm$ are defined as

$$K_\pm(\omega,\omega') = \int d\nu\, \alpha(\nu)^2 F(\nu) \times \left[\frac{1}{\omega'+\omega+\nu+i\eta} \pm \frac{1}{\omega'-\omega+\nu-i\eta}\right], \quad \text{(B·3)}$$

where $F(\nu)$ is the phonon density of states and $\alpha(\nu)$ is the effective electron–phonon coupling.[74] When we take $F(\nu) = \delta(\nu-\Omega)$ and $\alpha(\nu)^2 = N_n(0)g_{\mathrm{el-ph}}^2$, the kernel functions represent the Einstein model with the Einstein phonon frequency Ω and the dressed electron–phonon coupling constant $g_{\mathrm{el-ph}}$.

Appendix C: Vekhter–Varma Extension

Here, we briefly explain the Vekhter–Varma extension of the Migdal–Eliashberg–Nambu theory and the derivation of Eq. (38). First, the 11 component of the matrix representation Eq. (25) is rewritten as a function of $\delta k_\perp$, θ, and ω as

$$\begin{aligned} G_{11}(\delta k_\perp,\theta,\omega) &= \frac{Z(\delta k_\perp,\theta,\omega)\omega + \epsilon(\delta k_\perp,\theta)}{Z(\delta k_\perp,\theta,\omega)^2\omega^2 - \epsilon(\delta k_\perp)^2 - \phi(\delta k_\perp,\theta,\omega)^2} \\ &= \frac{1}{Z(\delta k_\perp,\theta,\omega)} \frac{\omega+\xi(\delta k_\perp,\theta,\omega)}{\omega^2-\xi(\delta k_\perp,\theta,\omega)^2-\Delta(\delta k_\perp,\theta,\omega)^2}, \end{aligned} \quad \text{(C·1)}$$

where $\xi = \epsilon/Z$ and $\Delta = \phi/Z$.

Then, we integrate the Green function along $\delta k_\perp$ as

$$\int G_{11}(\delta k_\perp,\theta,\omega)\, d\delta\, k_\perp = f(\theta,\omega) - i\pi N_s(\theta,\omega), \quad \text{(C·2)}$$

where $f(\theta,\omega)$ and $-\pi N_s(\theta,\omega)$ are the real and imaginary part of the integration, respectively.

When $Z(k_\perp,\theta,\omega)$ and $\Delta(k_\perp,\theta,\omega)$ are $k_\perp$ independent, the integral in the right hand side of Eq. (C·2) is transformed as

$$\int G_{11}(\delta k_\perp,\theta,\omega)\, d\delta\, k_\perp = \int G_{11}(\delta k_\perp,\theta,\omega) \frac{Z(\theta,\omega)}{v(\xi,\theta,\omega)}\, d\xi, \quad \text{(C·3)}$$

where the velocity $v(\xi,\theta,\omega)$ is given by

$$v(\xi,\theta,\omega) = \left.\frac{\partial\epsilon}{\partial\delta k_\perp}\right|_{\epsilon(\delta k_\perp)/Z=\xi}. \quad \text{(C·4)}$$

Then, the integration Eq. (C·3) is transformed as

$$\begin{aligned} &\int G_{11}(\delta k_\perp,\theta,\omega)\frac{Z(\theta,\omega)}{v(\xi,\theta,\omega)}\, d\xi \\ &= \int \frac{\omega+\xi}{\omega^2-\Delta(\theta,\omega)^2-\xi^2}\frac{d\xi}{v(\xi,\theta,\omega)}. \end{aligned} \quad \text{(C·5)}$$

Only when there is a $\epsilon_{\mathrm{cutoff}}$ that satisfies $v(\xi,\theta,\omega) \simeq v_F(\theta)$ ($v_F \in \mathbb{R}$) for $|\xi| < |\epsilon_{\mathrm{cutoff}}/Z|$ and $\max(|\omega^2-\Delta^2|,\omega^2) \ll |\epsilon_{\mathrm{cutoff}}/Z|^2$, the right hand side of Eq. (C·5) leads to

$$\begin{aligned} &\int \frac{\omega+\xi}{\omega^2-\Delta(\theta,\omega)^2-\xi}\frac{d\xi}{v(\xi,\theta,\omega)} \\ &\simeq \frac{1}{v_F(\theta)}\int_{-\infty}^{+\infty}\frac{\omega+\xi}{[a(\theta,\omega)+ib(\theta,\omega)]^2-\xi^2}\, d\xi, \end{aligned} \quad \text{(C·6)}$$

where $a+ib = \sqrt{\omega^2-\Delta^2}$. By integrating ξ as

$$\int_{-\infty}^{+\infty}\frac{\omega+\xi}{(a+ib)^2-\xi^2}\, d\xi = -\pi i\frac{\omega}{a+ib}, \quad \text{(C·7)}$$

we obtain

$$f(\theta,\omega) - i\pi N_s(\theta,\omega) \simeq -\frac{\pi i}{v_F(\theta)}\frac{\omega}{a+ib}. \quad \text{(C·8)}$$

Thus, the partially spectral function in the superconducting state is given by

$$N_s(\theta,\omega) \simeq \frac{1}{v_F(\theta)}\mathrm{Re}\left[\frac{\omega}{\sqrt{\omega^2-\Delta(\theta,\omega)^2}}\right], \quad \text{(C·9)}$$

while $N_n(\theta,\omega) = 1/v_F(\theta)$. We should note that, even when Z depends on temperatures, v_F is independent of the temperature since v_F is nothing but the Fermi velocity of the bare band dispersion ϵ.

*YAMAJI.Youhei@nims.go.jp

1) J. J. de Pablo, N. E. Jackson, M. A. Webb, L.-Q. Chen, J. E. Moore, D. Morgan, R. Jacobs, T. Pollock, D. G. Schlom, E. S. Toberer, J. Analytis, I. Dabo, D. M. DeLongchamp, G. A. Fiete, G. M. Grason, G. Hautier, Y. Mo, K. Rajan, E. J. Reed, E. Rodriguez, V. Stevanovic, J. Suntivich, K. Thornton, and J.-C. Zhao, npj Comput. Mater. **5**, 41 (2019).
2) A. Gelman, J. B. Carlin, H. S. Stern, and D. B. Rubin, *Bayesian Data Analysis* (Chapman & Hall/CRC, London, 1995).
3) S. Theodoridis, *Machine Learning—A Bayesian and Optimization Perspective* (Academic Press, London, 2015).
4) Many databases for materials have been developed. Even when limited to inorganic crystals, there are a considerable number of databases. A typical one provides crystal strucutres for a given conditions, for example, a set of atomic spieces, or a part of chemical formula. Sometime, stability of those structures are only tested by *ab initio* simulations. Examples of databases for inorganic materials would be ICSD,[149] Materials Project,[150] AFLOW, MatNavi, and topological materials database.[151–154]
5) G. Pizzi, A. Cepellotti, R. Sabatini, N. Marzari, and B. Kozinsky, Comput. Mater. Sci. **111**, 218 (2016).
6) G. Carleo and M. Troyer, Science **355**, 602 (2017).
7) J. Liu, Y. Qi, Z. Y. Meng, and L. Fu, Phys. Rev. B **95**, 041101 (2017).
8) S.-H. Li, C.-X. Dong, L. Zhang, and L. Wang, Phys. Rev. X **10**, 021020 (2020).
9) J. R. Schrieffer, *Theory of Superconductivity* (CRC Press, Boca Raton, FL, 2018).
10) T. Matsumura, N. Nagamura, S. Akaho, K. Nagata, and Y. Ando, Sci. Technol. Adv. Mater. **20**, 733 (2019).
11) M. Shiga and S. Muto, e-J. Surf. Sci. Nanotechnol. **17**, 148 (2019).
12) Y. Kim, D. Oh, S. Huh, D. Song, S. Jeong, J. Kwon, M. Kim, D. Kim, H. Ryu, J. Jung, W. Kyung, B. Sohn, S. Lee, J. Hyun, Y. Lee, Y. Kim, and C. Kim, Rev. Sci. Instrum. **92**, 073901 (2021).
13) F. Restrepo, J. Zhao, and U. Chatterjee, Rev. Sci. Instrum. **93**, 065106 (2022).
14) J. Liu, D. Huang, Y.-f. Yang, and T. Qian, Phys. Rev. B **107**, 165106 (2023).
15) J. Skilling, *Maximum Entropy and Bayesian Methods: Cambridge, England, 1988* (Springer Science+Business Media, Dordrecht, 2013) p. 455.
16) H. Shao and A. W. Sandvik, Phys. Rep. **1003**, 1 (2023).
17) P. A. M. Dirac, Proc. R. Soc. Lond., Ser. A **112**, 661 (1926).
18) J. C. Slater, Phys. Rev. **32**, 339 (1928).
19) M. Imada, A. Fujimori, and Y. Tokura, Rev. Mod. Phys. **70**, 1039 (1998).
20) N. Mott, *Metal–Insulator Transitions* (CRC Press, Boca Raton, FL, 2004).
21) M. A. Kastner, R. J. Birgeneau, G. Shirane, and Y. Endoh, Rev. Mod. Phys. **70**, 897 (1998).
22) R. P. Feynman and M. Cohen, Phys. Rev. **102**, 1189 (1956).
23) R. P. Feynman, Phys. Rev. **94**, 262 (1954).

24) D. Pines, Phys. Today **42** [2], 61 (1989).
25) L. D. Landau, Sov. Phys. JETP **3**, 920 (1957).
26) D. Pines and P. Nozières, *The Theory of Quantum Liquids* (Perseus Books Publishing, New York, 1999).
27) A. Damascelli, Z. Hussain, and Z.-X. Shen, Rev. Mod. Phys. **75**, 473 (2003).
28) J. A. Sobota, Y. He, and Z.-X. Shen, Rev. Mod. Phys. **93**, 025006 (2021).
29) E. L. Shirley, Phys. Rev. B **54**, 7758 (1996).
30) H. Maebashi and Y. Takada, Phys. Rev. B **84**, 245134 (2011).
31) Y. Pavlyukh, A.-M. Uimonen, G. Stefanucci, and R. van Leeuwen, Phys. Rev. Lett. **117**, 206402 (2016).
32) M. Charlebois and M. Imada, Phys. Rev. X **10**, 041023 (2020).
33) D. Sénéchal, D. Perez, and M. Pioro-Ladriere, Phys. Rev. Lett. **84**, 522 (2000).
34) M. Kohno, Phys. Rev. Lett. **105**, 106402 (2010).
35) C. Yang and A. E. Feiguin, Phys. Rev. B **93**, 081107 (2016).
36) A. Kreisel, P. Choubey, T. Berlijn, W. Ku, B. M. Andersen, and P. J. Hirschfeld, Phys. Rev. Lett. **114**, 217002 (2015).
37) N. Marzari and D. Vanderbilt, Phys. Rev. B **56**, 12847 (1997).
38) I. Souza, N. Marzari, and D. Vanderbilt, Phys. Rev. B **65**, 035109 (2001).
39) O. K. Andersen, A. I. Liechtenstein, O. Jepsen, and F. Paulsen, J. Phys. Chem. Solids **56**, 1573 (1995).
40) M. Hirayama, Y. Yamaji, T. Misawa, and M. Imada, Phys. Rev. B **98**, 134501 (2018).
41) J.-B. Morée, M. Hirayama, M. T. Schmid, Y. Yamaji, and M. Imada, Phys. Rev. B **106**, 235150 (2022).
42) V. Meden and K. Schönhammer, Phys. Rev. B **46**, 15753 (1992).
43) J. Voit, Phys. Rev. B **47**, 6740 (1993).
44) H. J. Schulz, G. Cuniberti, and P. Pieri, Fermi Liquids and Luttinger Liquids, *Field Theories for Low-Dimensional Condensed Matter Systems: Spin Systems and Strongly Correlated Electrons* (Springer, Berlin/Heidelberg, 2000) p. 9.
45) C. N. Yang, Rev. Mod. Phys. **34**, 694 (1962).
46) B. Kyung, D. Sénéchal, and A.-M. S. Tremblay, Phys. Rev. B **80**, 205109 (2009).
47) Y. Nambu, Phys. Rev. **117**, 648 (1960).
48) A. Abrikosov, *Methods of Quantum Field Theory in Statistical Physics*.
49) A. L. Fetter and J. D. Walecka, *Quantum Theory of Many-particle Systems* (Courier Corporation, 2012).
50) J. M. Luttinger and J. C. Ward, Phys. Rev. **118**, 1417 (1960).
51) R. Jastrow, Phys. Rev. **98**, 1479 (1955).
52) M. C. Gutzwiller, Phys. Rev. Lett. **10**, 159 (1963).
53) W. L. McMillan, Phys. Rev. **138**, A442 (1965).
54) D. Ceperley, G. V. Chester, and M. H. Kalos, Phys. Rev. B **16**, 3081 (1977).
55) R. B. Laughlin, Phys. Rev. Lett. **50**, 1395 (1983).
56) Y. Yanase, T. Jujo, T. Nomura, H. Ikeda, T. Hotta, and K. Yamada, Phys. Rep. **387**, 1 (2003).
57) S. Shinkai, H. Ikeda, and K. Yamada, J. Phys. Soc. Jpn. **74**, 2592 (2005).
58) N. E. Bickers, D. J. Scalapino, and S. R. White, Phys. Rev. Lett. **62**, 961 (1989).
59) N. V. Prokof'ev, B. V. Svistunov, and I. S. Tupitsyn, J. Exp. Theor. Phys. **87**, 310 (1998).
60) L. Hedin, Phys. Rev. **139**, A796 (1965).
61) Y. Takada, Phys. Rev. Lett. **87**, 226402 (2001).
62) E. Müller-Hartmann, Z. Phys. B **74**, 507 (1989).
63) W. Metzner and D. Vollhardt, Phys. Rev. Lett. **62**, 324 (1989).
64) A. Georges, G. Kotliar, W. Krauth, and M. J. Rozenberg, Rev. Mod. Phys. **68**, 13 (1996).
65) G. Kotliar, S. Y. Savrasov, K. Haule, V. S. Oudovenko, O. Parcollet, and C. A. Marianetti, Rev. Mod. Phys. **78**, 865 (2006).
66) S. Sakai, J. Phys. Soc. Jpn. **92**, 092001 (2023).
67) J. Kaufmann, C. Eckhardt, M. Pickem, M. Kitatani, A. Kauch, and K. Held, Phys. Rev. B **103**, 035120 (2021).
68) H. Park, K. Haule, and G. Kotliar, Phys. Rev. Lett. **107**, 137007 (2011).
69) J. Bardeen, L. N. Cooper, and J. R. Schrieffer, Phys. Rev. **106**, 162 (1957).
70) A. B. Migdal, Sov. Phys. JETP **7**, 996 (1958).
71) G. Eliashberg, Sov. Phys. JETP **11**, 696 (1960).
72) J. R. Schrieffer, D. J. Scalapino, and J. W. Wilkins, Phys. Rev. Lett. **10**, 336 (1963).
73) D. J. Scalapino, J. R. Schrieffer, and J. W. Wilkins, Phys. Rev. **148**, 263 (1966).
74) W. L. McMillan and J. M. Rowell, Phys. Rev. Lett. **14**, 108 (1965).
75) J. M. Rowell, W. L. McMillan, and W. L. Feldmann, Phys. Rev. B **3**, 4065 (1971).
76) I. Vekhter and C. M. Varma, Phys. Rev. Lett. **90**, 237003 (2003).
77) C. M. Varma, P. B. Littlewood, S. Schmitt-Rink, E. Abrahams, and A. E. Ruckenstein, Phys. Rev. Lett. **63**, 1996 (1989).
78) K.-Y. Yang, T. M. Rice, and F.-C. Zhang, Phys. Rev. B **73**, 174501 (2006).
79) Y. Yamaji and M. Imada, Phys. Rev. Lett. **106**, 016404 (2011).
80) S. Sakai, M. Civelli, and M. Imada, Phys. Rev. Lett. **116**, 057003 (2016).
81) A. V. Chubukov and J. Schmalian, Phys. Rev. B **101**, 180510 (2020).
82) E. Mascot, A. Nikolaenko, M. Tikhanovskaya, Y.-H. Zhang, D. K. Morr, and S. Sachdev, Phys. Rev. B **105**, 075146 (2022).
83) S. Sakai, Y. Motome, and M. Imada, Phys. Rev. Lett. **102**, 056404 (2009).
84) Y. Yamaji and M. Imada, Phys. Rev. B **83**, 214522 (2011).
85) J. Maldacena, Int. J. Theor. Phys. **38**, 1113 (1999).
86) J. Zaanen, SciPost Phys. **6**, 061 (2019).
87) S. S. Gubser and F. D. Rocha, Phys. Rev. D **81**, 046001 (2010).
88) S. S. Gubser and J. Ren, Phys. Rev. D **86**, 046004 (2012).
89) S. Smit, E. Mauri, L. Bawden, F. Heringa, F. Gerritsen, E. van Heumen, Y. K. Huang, T. Kondo, T. Takeuchi, N. E. Hussey, M. Allan, T. K. Kim, C. Cacho, A. Krikun, K. Schalm, H. T. C. Stoof, and M. S. Golden, Nat. Commun. **15**, 4581 (2024).
90) D. H. Ackley, G. E. Hinton, and T. J. Sejnowski, Cognitive Sci. **9**, 147 (1985).
91) P. Smolensky, Information Processing in Dynamical Systems: Foundations of Harmony Theory, in *Parallel Distributed Processing: Explorations in the Microstructure of Cognition*, ed. D. E. Rumelhart, J. L. McClelland, and the PDP Research Group (MIT Press, Cambridge, MA, 1986) Foundations, Vol. 1, p. 194.
92) Y. Nomura, A. S. Darmawan, Y. Yamaji, and M. Imada, Phys. Rev. B **96**, 205152 (2017).
93) Y. Yamaji, T. Yoshida, A. Fujimori, and M. Imada, Phys. Rev. Res. **3**, 043099 (2021).
94) S. G. Mallat, IEEE Trans. Pattern Anal. Mach. Intell. **11**, 674 (1989).
95) S. Mallat, *A Wavelet Tour of Signal Processing: The Sparse Way* (Academic Press, Burlington, 2009).
96) H. Shinaoka, M. Wallerberger, Y. Murakami, K. Nogaki, R. Sakurai, P. Werner, and A. Kauch, Phys. Rev. X **13**, 021015 (2023).
97) K. Hornik, M. Stinchcombe, and H. White, Neural Networks **2**, 359 (1989).
98) S.-I. Amari, Neural Comput. **10**, 251 (1998).
99) C. M. Bishop, *Pattern Recognition and Machine Learning* (Springer, Berlin, 2006).
100) Y. Freund and D. Haussler, Advances in Neural Information Processing Systems, 1991, Vol. 4.
101) N. Le Roux and Y. Bengio, Neural Comput. **20**, 1631 (2008).
102) J. M. Bok, J. J. Bae, H.-Y. Choi, C. M. Varma, W. Zhang, J. He, Y. Zhang, L. Yu, and X.-J. Zhou, Sci. Adv. **2**, e1501329 (2016).
103) A. W. Sandvik, D. J. Scalapino, and N. E. Bickers, Phys. Rev. B **69**, 094523 (2004).
104) T. P. Devereaux, T. Cuk, Z.-X. Shen, and N. Nagaosa, Phys. Rev. Lett. **93**, 117004 (2004).
105) Z. Li, M. Wu, Y.-H. Chan, and S. G. Louie, Phys. Rev. Lett. **126**, 146401 (2021).
106) I. A. Nekrasov, K. Held, G. Keller, D. E. Kondakov, Th. Pruschke, M. Kollar, O. K. Andersen, V. I. Anisimov, and D. Vollhardt, Phys. Rev. B **73**, 155112 (2006).
107) K. Byczuk, M. Kollar, K. Held, Y.-F. Yang, I. A. Nekrasov, Th. Pruschke, and D. Vollhardt, Nat. Phys. **3**, 168 (2007).
108) K. Held, R. Peters, and A. Toschi, Phys. Rev. Lett. **110**, 246402 (2013).
109) X. J. Zhou, J. Shi, T. Yoshida, T. Cuk, W. L. Yang, V. Brouet, J. Nakamura, N. Mannella, S. Komiya, Y. Ando, F. Zhou, W. X. Ti, J. W. Xiong, Z. X. Zhao, T. Sasagawa, T. Kakeshita, H. Eisaki, S. Uchida, A. Fujimori, Z. Zhang, E. W. Plummer, R. B. Laughlin, Z.

Hussain, and Z.-X. Shen, Phys. Rev. Lett. **95**, 117001 (2005).
110) L. L. Lev, I. O. Maiboroda, M.-A. Husanu, E. S. Grichuk, N. K. Chumakov, I. S. Ezubchenko, I. A. Chernykh, X. Wang, B. Tobler, T. Schmitt, M. L. Zanaveskin, V. G. Valeyev, and V. N. Strocov, Nat. Commun. **9**, 2653 (2018).
111) P. O. Gartland and B. J. Slagsvold, Phys. Rev. B **12**, 4047 (1975).
112) S. D. Kevan and R. H. Gaylord, Phys. Rev. B **36**, 5809 (1987).
113) F. Reinert, G. Nicolay, S. Schmidt, D. Ehm, and S. Hüfner, Phys. Rev. B **63**, 115415 (2001).
114) A. Tamai, W. Meevasana, P. D. C. King, C. W. Nicholson, A. de la Torre, E. Rozbicki, and F. Baumberger, Phys. Rev. B **87**, 075113 (2013).
115) M. Hengsberger, R. Frésard, D. Purdie, P. Segovia, and Y. Baer, Phys. Rev. B **60**, 10796 (1999).
116) J. B. Hannon and E. W. Plummer, J. Electron Spectrosc. Relat. Phenom. **64–65**, 683 (1993).
117) M. Hengsberger, D. Purdie, P. Segovia, M. Garnier, and Y. Baer, Phys. Rev. Lett. **83**, 592 (1999).
118) K. Morikawa, T. Mizokawa, K. Kobayashi, A. Fujimori, H. Eisaki, S. Uchida, F. Iga, and Y. Nishihara, Phys. Rev. B **52**, 13711 (1995).
119) A. Sekiyama, H. Fujiwara, S. Imada, S. Suga, H. Eisaki, S. I. Uchida, K. Takegahara, H. Harima, Y. Saitoh, I. A. Nekrasov, G. Keller, D. E. Kondakov, A. V. Kozhevnikov, Th. Pruschke, K. Held, D. Vollhardt, and V. I. Anisimov, Phys. Rev. Lett. **93**, 156402 (2004).
120) S. Aizaki, T. Yoshida, K. Yoshimatsu, M. Takizawa, M. Minohara, S. Ideta, A. Fujimori, K. Gupta, P. Mahadevan, K. Horiba, H. Kumigashira, and M. Oshima, Phys. Rev. Lett. **109**, 056401 (2012).
121) J. M. Tomczak, M. Casula, T. Miyake, and S. Biermann, Phys. Rev. B **90**, 165138 (2014).
122) F. Reinert, D. Ehm, S. Schmidt, G. Nicolay, S. Hüfner, J. Kroha, O. Trovarelli, and C. Geibel, Phys. Rev. Lett. **87**, 106401 (2001).
123) A. Shimoyamada, S. Tsuda, K. Ishizaka, T. Kiss, T. Shimojima, T. Togashi, S. Watanabe, C. Q. Zhang, C. T. Chen, Y. Matsushita, H. Ueda, Y. Ueda, and S. Shin, Phys. Rev. Lett. **96**, 026403 (2006).
124) T. Kondo, W. Malaeb, Y. Ishida, T. Sasagawa, H. Sakamoto, T. Takeuchi, T. Tohyama, and S. Shin, Nat. Commun. **6**, 7699 (2015).
125) A. L. Cavalieri, N. Müller, Th. Uphues, V. S. Yakovlev, A. Baltuška, B. Horvath, B. Schmidt, L. Blümel, R. Holzwarth, S. Hendel, M. Drescher, U. Kleineberg, P. M. Echenique, R. Kienberger, F. Krausz, and U. Heinzmann, Nature **449**, 1029 (2007).
126) J. K. Freericks, H. R. Krishnamurthy, and Th. Pruschke, Phys. Rev. Lett. **102**, 136401 (2009).
127) T. Kondo, Y. Hamaya, A. D. Palczewski, T. Takeuchi, J. Wen, Z. Xu, G. Gu, J. Schmalian, and A. Kaminski, Nat. Phys. **7**, 21 (2011).
128) J. M. Rowell, P. W. Anderson, and D. E. Thomas, Phys. Rev. Lett. **10**, 334 (1963).
129) A. Chainani, T. Yokoya, T. Kiss, and S. Shin, Phys. Rev. Lett. **85**, 1966 (2000).
130) D. L. Price, Proc. R. Soc. Lond., Ser. A **300**, 25 (1967).
131) J. M. Rowe, Phys. Rev. **163**, 547 (1967).
132) J. P. Carbotte, Rev. Mod. Phys. **62**, 1027 (1990).
133) M. R. Norman, H. Ding, H. Fretwell, M. Randeria, and J. C. Campuzano, Phys. Rev. B **60**, 7585 (1999).
134) H. Li, X. Zhou, S. Parham, T. J. Reber, H. Berger, G. B. Arnold, and D. S. Dessau, Nat. Commun. **9**, 26 (2018).
135) G. Binnig and H. Rohrer, Rev. Mod. Phys. **59**, 615 (1987).
136) L. Petersen, P. T. Sprunger, Ph. Hofmann, E. Lægsgaard, B. G. Briner, M. Doering, H.-P. Rust, A. M. Bradshaw, F. Besenbacher, and E. W. Plummer, Phys. Rev. B **57**, R6858 (1998).
137) J. E. Hoffman, K. McElroy, D.-H. Lee, K. M. Lang, H. Eisaki, S. Uchida, and J. C. Davis, Science **297**, 1148 (2002).
138) T. Machida, Y. Kohsaka, and T. Hanaguri, Rev. Sci. Instrum. **89**, 093707 (2018).
139) T. Hanaguri and Y. Kohsaka, *Spectroscopic-imaging Scanning Tunneling Microscopy* (Kyoritsu, Tokyo, 2023) [in Japanese].
140) A. Kotani and S. Shin, Rev. Mod. Phys. **73**, 203 (2001).
141) L. J. P. Ament, M. van Veenendaal, T. P. Devereaux, J. P. Hill, and J. van den Brink, Rev. Mod. Phys. **83**, 705 (2011).
142) K. Tsutsui, T. Tohyama, and S. Maekawa, Phys. Rev. B **61**, 7180 (2000).
143) T. Misawa, S. Morita, K. Yoshimi, M. Kawamura, Y. Motoyama, K. Ido, T. Ohgoe, M. Imada, and T. Kato, Comput. Phys. Commun. **235**, 447 (2019).
144) E. Manousakis, Rev. Mod. Phys. **63**, 1 (1991).
145) T. Momoi and K. Totsuka, Phys. Rev. B **62**, 15067 (2000).
146) H. Shao, Y. Q. Qin, S. Capponi, S. Chesi, Z. Y. Meng, and A. W. Sandvik, Phys. Rev. X **7**, 041072 (2017).
147) N. N. Bogoljubov, V. V. Tolmachov, and D. V. Širkov, Fortschr. Phys. **6**, 605 (1958).
148) P. Morel and P. W. Anderson, Phys. Rev. **125**, 1263 (1962).
149) D. Zagorac, H. Müller, S. Ruehl, J. Zagorac, and S. Rehme, J. Appl. Crystallogr. **52**, 918 (2019).
150) A. Jain, S. P. Ong, G. Hautier, W. Chen, W. D. Richards, S. Dacek, S. Cholia, D. Gunter, D. Skinner, G. Ceder, and K. A. Persson, APL Mater. **1**, 011002 (2013).
151) B. Bradlyn, L. Elcoro, J. Cano, M. G. Vergniory, Z. Wang, C. Felser, M. I. Aroyo, and B. A. Bernevig, Nature **547**, 298 (2017).
152) M. G. Vergniory, L. Elcoro, C. Felser, N. Regnault, B. A. Bernevig, and Z. Wang, Nature **566**, 480 (2019).
153) M. G. Vergniory, B. J. Wieder, L. Elcoro, S. S. P. Parkin, C. Felser, B. A. Bernevig, and N. Regnault, Science **376**, eabg9094 (2022).
154) Web [https://www.cryst.ehu.es/].

Youhei Yamaji was born in Tokyo, Japan, in 1981. He received D.Eng. in 2010 from The University of Tokyo. He was a postdoctoral researcher at Rutgers (2010), a specially appointed research associate (2011–2014), a specially appointed lecturer (2014–2016), a specially appointed associate professor (2016–2021) at The University of Tokyo, and a senior researcher (2021–2023) at National Institute for Materials Science. He is now a group leader at Research Center for Materials Nanoarchitectonics, National Institute for Materials Science. He has been working on condensed matter theory and computational physics.